AFM Indentation Measurements and Viability Tests on Drug Treated Leukemia Cells

By
Hélène Fortier
Biomedical Engineering M.A.Sc.

Supervisor: Shan Zou
Co-supervisor: Fabio Variola

uOttawa

Université d'Ottawa ■ University of Ottawa
Department of Biomedical Mechanical Engineering
Faculty of Graduate and Postdoctoral Studies

TABLE OF CONTENTS

LIST OF ABBREVIATIONS

AFM	Atomic force microscopy
AML	Acute myelocytic leukemia
APL	Acute promyelocytic leukemia
ATO	Arsenic trioxide
ATRA	All-trans retinoic acid
AVG	Average
BGD	Background
DMEM	Dulbecco's Modified Eagle's Medium
EthD-1	Ethidium homodimer-1
FBS	Fetal bovine serum
H_2O	Water
H_2O_2	Hydrogen peroxide
H_2SO_4	Sulfuric acid
Max	Maximum
Min	Minimum
PBS	Phosphate buffered saline
SD	Standard deviation
UV	Ultraviolet

LIST OF FIGURES

LIST OF TABLES

ACKNOWLEDGMENTS

I would like to express my sincere gratitude to my thesis supervisor, Dr. Shan Zou, who has consistently inspired this study and provided valuable guidance and recommendations. Her endless patience and encouragements through the past years have concretized this Thesis. I have also acquired valuable research abilities through her instructions. My sincere thanks also go to Professor Fabio Variola, my thesis co-supervisor. He has provided extensive, professional and constructive suggestions on the structure and content of the Thesis.

Besides, I am grateful to Dr. Maohui Chen for the help in preparing SU8-10 substrates, and Chen Wang for his valuable proposal in assessing NB4 cell lines. Furthermore, I heartily thank the Measurement Science and Standards group from the National Research Council for their cooperation in conducting this research and for this outstanding research experience among their group.

Sincere gratitude should be given to the National Research Council of Canada (NRC), the Natural Sciences and Engineering Research Council (NSERC) as well as the University of Ottawa for their financial support.

ABSTRACT

A significant body of literature has reported strategies and techniques to assess the mechanical properties of biological samples such as proteins, cellular and tissue systems. Atomic force microscopy has been used to detect elasticity changes of cancer cells. However, only a few studies have provided a detailed and complete protocol of the experimental procedures and data analysis methods for non-adherent blood cancer cells. In this work, the elasticity of NB4 cells derived from acute promyelocytic leukemia (APL) was probed by AFM indentation measurements to investigate the effects of the disease on cellular biomechanics. Understanding how leukemia influences the nanomechanical properties of cells is expected to provide a better understanding of the cellular mechanisms associated to cancer, and promises to become a valuable new tool for cancer detection and staging. In this context, the quantification of the mechanical properties of APL cells requires a systematic and optimized approach for data collection and analysis, in order to generate reproducible and comparative data.

This Thesis elucidates the automated data analysis process that integrates programming, force curve collection and analysis optimization to assess variations of cell elasticity in response to processing criteria. A processing algorithm was developed by using the IGOR Pro software to automatically analyze large numbers of AFM data sets in an efficient and accurate manner. In fact, since the analysis involves multiple steps that must be repeated for many individual cells, an automated and un-biased processing approach is essential to precisely determine cell elasticity. Different fitting models for extracting the Young's modulus have been systematically applied to validate the process, and the best fitting criteria, such as the contact point location and indentation length, have been determined in order to obtain consistent results.

The designed automated processing code described in this Thesis was used to correlate alterations in cellular biomechanics of cancer cells as they undergo drug treatments. In order to fully assess drug effects on NB4 cells, viability assays were first performed using Trypan Blue staining for primary insights before initiating thorough microplate fluorescence intensity readings using a LIVE/DEAD viability kit involving ethidium and calcein AM labelling components. From 0 to 24 h after treatment using 30 μM arsenic trioxide, relative live cell populations increased until 36 h. From 0 to 12 h post-treatment, relative populations of dead cells increased until 24 h post-treatment. Furthermore, a drastic drop in dead cell count has been observed between 12 and 24 h. Additionally, arsenic trioxide drug induced alterations in elasticity of NB4 cells can be correlated to the cell viability tests.

With respect to cell mechanics, trapping of the non-adherent NB4 cells within fabricated SU8-10 microwell arrays, allowed consistent AFM indentation measurements up to 48 h after treatment. Results revealed an increase in cell elasticity up to 12 h post-treatment and a drastic decrease between 12 and 24 h. Furthermore, arsenic trioxide drug induced alterations in elasticity of NB4 cells can be correlated to the cell viability tests.

In addition to these indentation and viability testing approaches, morphological appearances were monitored, in order to track the apoptosis process of the affected cells. Relationships found between viability and elasticity assays in conjunction with morphology alterations revealed distinguish stages of apoptosis throughout treatment. 24 h after initial treatment, most cells were observed to have burst or displayed obvious blebbing. These relations between different measurement methods may reveal a potential drug screening approach, for understanding specific physical and biological of drug effects on the cancer cells.

Keywords: atomic force microscopy, cancer cell mechanics, leukemia, automated data processing.

CHAPTER 1: INTRODUCTION

1.1 Objectives and Motivation

1.1.1 Objectives

Changes in cell structure and mechanics, as well as alterations of the cellular response to external stimuli (mechanotransduction) are associated with the development of many diseases, including cancer[1,2]. *In vitro* experiments have in fact shown that the cytoskeletal architecture and mechanical properties of cancer and healthy cells are significantly different. For example, specific cell lines of breast, pancreatic and brain cancers exhibit much lower viscoelastic properties than non-cancerous cells[3,4]. Similarly, epithelial cancer cells are characterized by a stiffer structure than that of healthy cells[5]. While these previous studies showed that biomechanical variations are cell-dependent and can thus not be generalized across different cell lines, they nonetheless highlight the importance of biomechanics for sorting and identifying cancer cells, thereby promising to play an important role in cancer detection and staging.

To date, several experimental approaches have been employed to quantify the cytoskeletal stiffness and assess the Young's modulus, or elastic modulus, of individual cells[6,7]. Among these, the exploitation of magnetic beads and the use of cellular indentation techniques such as cytoindentation and atomic force microscopy (AFM) have permitted to precisely determine cellular biomechanics[6,8,9]. However, current literature on the subject does not always discuss the precise details of the experimental procedures and data analysis approaches related to special non-adherent cells such as white blood cells. Access to this information is crucial for peers interested in reproducing the measurements of the elastic modulus of single cells by using specific and consistent measurement parameters, such as applied force, *z*-scan length and range,

as well as detailed information to recreate the experimental conditions, since minimal experimental variations may lead to different conclusions. This Thesis addresses this matter by thoroughly outlining the experimental and analytical procedure to assess the elastic response of human acute promyelocytic leukemia (APL) derived NB4 cells when undergoing drug-induced elasticity alterations. In particular, this Thesis aims at achieving the following objectives:

1) Optimize AFM data collection and analysis procedures, in order to create an automated batch analysis code specific to NB4 cells.
2) Assess viability, morphology and elasticity measurements and correlate them to apoptosis.

1.1.2 Relevance

Elasticity measurements using AFM have already been performed over HL60 (derived from acute myeloid leukemia) and Jurkat cell lines (derived from acute lymphocytic leukemia)[10] uncovering that myeloid leukemia cells were stiffer than lymphoid leukemia cells, which is in agreement with the higher leukostasis rate involved in myeloid leukemia. However, as APL is a serious type of leukemia that has transformed from highly fatal to highly curable[11,12], NB4 cell lines are of great interest in this study. Effective treatments for patients with APL suggest that drug induced alterations should be observable early and throughout treatments. In addition, NB4 cell elasticity has not yet been monitored and may serve as an example and baseline in linking viability, elasticity and morphology changes upon treatment. These experiments will provide a better understanding of drug effects and cancer cell mechanics.

1.2 Background

1.2.1 Leukemia

Leukemia is the cancer of blood forming tissue such as bone marrow and causes a large build-up of white blood cells with chromosomal translocations regulating its behavior. Different types of leukemia are classified according to the type of white blood cells that proliferates, such as myeloid or lymphoid stem cells. Given the type of chromosomal translocation, it is also possible to label the type of leukemia as either acute or chronic in order to predict its behavior and define its treatment. Acute leukemia involves a rapid build-up of immature blood cells at an early phase of hematopoietic differentiation, while chronic leukemia grows in a slower manner as the abnormal proliferating cells eventually differentiate (or mature)[13,14].

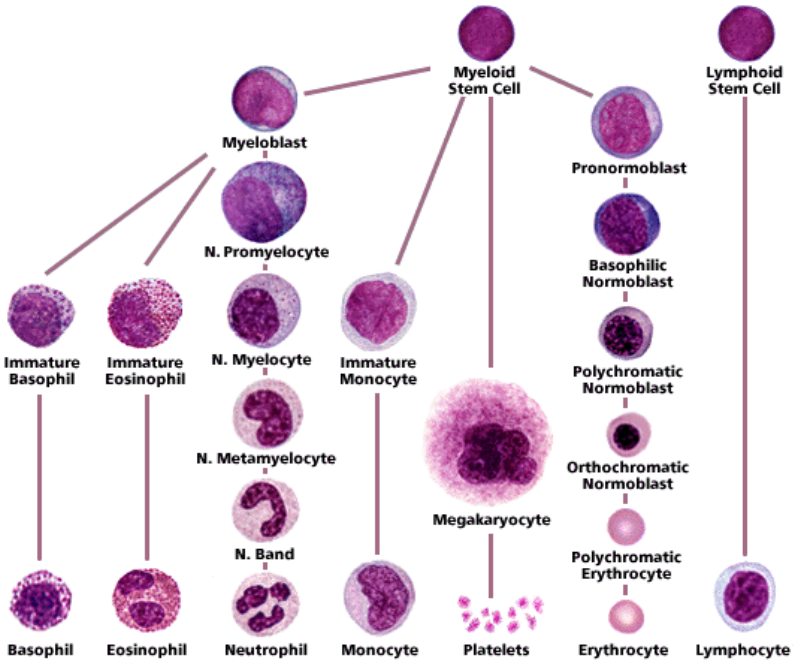

Figure 1. Simplified hematopoietic maturation chart of granulocytes (basophils, eosinophils and neutrophils), monocytes, platelets, erythrocytes and lymphocytes. Figure was adapted from reference 15.

In addition to these major types of leukemia, the disease also involves different subtypes identified according to the maturity of the affected cell during blood cell formation process, also known as hematopoiesis. Figure 1 displays a simplified chart of hematopoiesis by describing the different possible subtypes of immature granulocytes (basophils, eosinophils and neutrophils), monocytes, platelets, erythrocytes and lymphocytes. However, promyelocytes, myelocytes, metamyelocytes and bands are only identified in the differentiation process of neutrophils although they can be found through the maturation process of other granulocytes (eosinophils and basophils) derived from myeloblast. Noteworthy, it should be highlighted that the maturity levels of lymphocytes are not displayed in Figure 1, extending the complexity of the disease.

1.2.1.1 Diagnostic

Current hematologic diseases develop at the cellular level[16]. Although blood tests are fast procedures and allow identifying abnormal white blood cell counts suggesting leukemia, bone marrow aspiration or biopsy is often a painful procedure, however, required to confirm the diagnosis. A pathologist or hematologist then reviews the morphology of cells under microscope to identify the amount of immature and mature cells. Additionally, other lab tests such as fluorescence flow cytometry and cytochemistry are used to identify specific types of leukemia, *e.g*., acute or chronic; lymphocytic or myelocytic cells.

The fluorescence-based flow cytometry is also found useful in identifying the exact type of cells affected through the analysis of the recorded fluorescence intensity and antigen response patterns through antibody labelling. This technique has rapidly expanded from basic research to clinical laboratories, more prevalently in the diagnosis of blood cancer[17,18]. Flow cytometry allows the analysis of single suspension cells. Once the cells are labeled, they are introduced in a narrow laminar flow, separating the cells. When passing through a light source, cell fluorescence

is measured providing insights on the presence of specific DNA or protein, according to the labels used.

Modern flow cytometers include microfluidics in order to measure occlusion rates within the channels and evaluate cell coagulation[19]. Studies on leukemia cells have shown them to occlude microfluidic channels more rapidly than healthy cells[16,20]. Furthermore, HL60 cells affecting myeloblastic cells have been treated with different drugs (cytochalasin D and pentoxyfillin), in order to observe changes in cell deformability through flow cytometry[16]. Upon treatment, a larger amount of cells were found to pass through the fluidic system, indicating softening of the cells[21]. On the contrary, HL60 and Jurkat leukemia cells treated with daunorubicin and other chemotherapy drug exposure were found to increase cell stiffness[12] when probed using atomic force microscopy (AFM). However, as chemical and molecular components have been greatly investigated in diseases such as chromosome testing[22], fewer studies have investigated their mechanics[6,23,24] at the cellular level at which leukemia may be diagnosed.

1.2.1.2 Treatment

Different treatments for leukemia are available and chosen according to the diagnosed type of leukemia, chromosomal abnormalities, patient's age and overall health. Example of treatments may involve stem cell transplant and/or radiation therapy, as well as monoclonal antibody therapy in combination with chemotherapy. Acute promyelocytic leukemia (APL) is a unique subtype of acute myelocytic leukemia (AML), which represents 10% to 15% of all myelocytic leukemia. It is known to be treatable using retinoids to induce differentiation of the cells into mature granulocytes unlike other types of AML[11,25]. Many strategies for APL treatment have been investigated on NB4 cell lines derived from human APL to unravel medical breakthroughs. Esculetin[26], resveratrol[27] and daunorubicin[28] are only 3 of many different drugs

found to promote NB4 cell apoptosis alone or in combination therapy with arsenic trioxide (ATO)[29-31,]. In fact, the efficiency of the drug action depends on the induction of cell death, assessed using different viability tests such as flow cytometry.

Most of the above mentioned treatments are commonly known to introduce cancer cell death, which is generally discussed in terms of apoptosis or necrosis, involving different alterations in cell morphology[32,33]. Apoptosis is a programmed cell death that balances cell division in adult tissues. It involves cell shrinkage, pyknosis and karyorrhexis. Cell shrinkage occurs after initiation of apoptosis as caspase-3 cleaves DNA and the cytoskeleton of the cell. Then, the chromatin irreversibly condenses during pyknosis before the fragmentation of the nucleus (karyorrhexis) and disperses into apoptotic bodies among other components of the cell causing blebbing of the cell before it is phagocytosed. Necrosis on the other hand is found when a cell is injured (physically or chemically) and refers to the degradation process that occurs after cell death and is preceded by oncosis. Oncosis is a process involving dissolution of the chromatin (karyolysis) and cell swelling due to osmotic pressure in organelles[34]. In any case, once treated, cells undergo morphology alterations as they go through cell death processes[35,36]. These alterations may be monitored by visual inspection and fluorescence imaging, as well as through cell mechanics analysis.

The mechanism and action of ATO in effectively treating APL is still unclear, but is believed by its ability to induce apoptosis to control APL cell proliferation[37-42]. Worldwide treatments for APL include all-trans retinoic acid (ATRA), in combination with a chemotherapy drug[43-45]. Although not endorsed by Health Canada[46], ATO (or Trisenox) has been approved by the Australian Therapeutic Goods Administration in 2009[47], the United States Food and Drug Administration (FDA)[48] and the European Medicines Agency[49] for relapsed APL patients[50]. A

common treatment specific to APL patients involves ATRA in combination with ATO[51-54,] for elderly or frailer patients who are unable to tolerate chemotherapy drugs[55,56]. ATO is used in combination with ATRA since ATRA alone causes cancer relapse, as it stops myeloid differentiation at the promyelocytic stage but can't eliminate the leukemic clones created[43,57,58]. ATO, or Trisenox[59] treatment involves 2 phases: the first one is the induction therapy during which 0.15 mg/kg of a 10 mg/10 mL arsenic trioxide solution is administered intravenously over 1 to 2 h daily until bone marrow remission without exceeding 60 doses; the second phase is the consolidation therapy, during which the same dosage is administered daily for up to 5 weeks. For a patient of 60 kg, about 50 μM is administered daily for up to 95 days.

1.2.2 Atomic Force Microscopy (AFM)

In general, the AFM consists of a probe mounted on a flexible cantilever (AFM tip) which raster scans across a sample surface controlled by piezo based scanners in 3D. The recorded cantilever deflection by reflecting a laser spot on the backside of the cantilever into an array of photodiodes (photodetector) is used to create the topographic images. In addition to imaging capacities, this instrument also uniquely permits to efficiently characterize the elasticity of soft materials (*e.g.* cells and tissues) *via* force spectroscopy and/or force mapping, resulting in the ability to quantify the sample's mechanical response to controlled forces with sub nano Newton resolution[7,60-62]. Usually, the force measurements including force indentation experiments are carried out in the contact mode, and the *z*-piezo displacement can be used to control the cantilever's deflection (the applied force on the sample) and the indentation length.

1.2.2.1 Data Analysis

Analyzing the stiffness of hard materials with the AFM is usually performed by a simple linear fitting of force-distance curves that does not necessitate any offset of the raw indentation

data. On the other hand, because soft samples generate a non-linear response to external mechanical stimuli due to their viscoelastic properties[63-65], AFM data analysis and interpretation require a different approach.

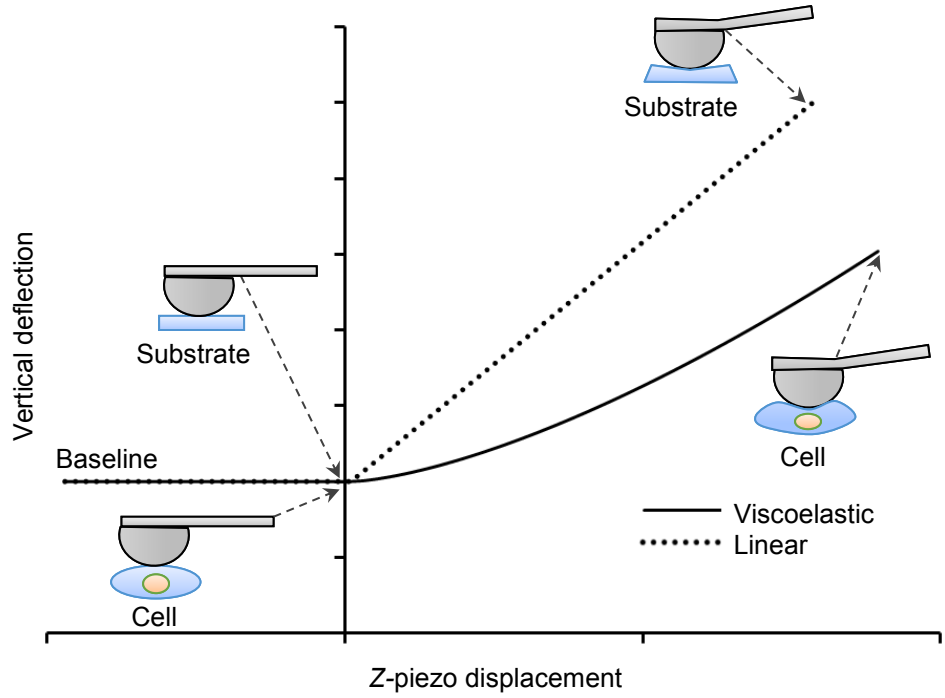

Figure 2. Cantilever vertical deflection versus *z*-piezo displacement curves during indentations of a single cell (solid line) and of an incompressible substrate (dotted line), respectively.

Figure 2 displays the deflection of the AFM cantilever as a function of the vertical displacement of the *z*-piezo device when indenting soft (*i.e.,* single cells) and hard materials. An incompressible or purely elastic material generates a linear relation between the cantilever deflection and the AFM's *z*-piezo displacement (dotted line in Figure 2). Conversely, during deformation, a cell behaves as a viscoelastic material, generating a nonlinear relationship between the cantilever deflection and the *z*-piezo displacement (solid line in Figure 2). In both cases, the analysis of force-indentation curves is carried out by employing contact mechanic

models which depends on the geometry of the probe used for indentation (*e.g.* spherical, conical).

These models derive from Hertz contact mechanics on the deformation of an elastic half-space indented by a conical shaped probe. They are used to extract Young's modulus values, which define the relationship between stress and strain (within the proportional/elastic region of a stress-strain curve) in a material. This mechanical property can be used to predict the behavior of a material upon elongation or compression. The effects of the probe's geometry are included by considering the Sneddon's approximation[66,67]. The resulting models encompass many assumptions including infinitesimal deformation, linearity of the half-space, infinite sample thickness, isotropic properties and flat (frictionless) contact surfaces. Additionally, they do not include parameters affecting the behavior of viscoelastic materials such as the loading rate. These assumptions do not perfectly reflect the characteristics of soft materials, but they may be, and have been used nonetheless for comparative analyses to investigate variations in the elastic properties of different samples in response to applied forces, given that the same type of probe and the same applied forces are used[68,69].

1.2.2.2 Challenges in Non-Adherent Cells

It should be noted that the AFM investigation of non-adherent cells such as NB4 cells is a challenging endeavor. In fact, imaging of cells usually requires chemical or biochemical immobilization to firmly fix them onto the substrate, a procedure that may however alter cell membrane structures and thus their mechanical properties. Therefore, in order to avoid these limitations, microwell arrays were used to physically confine NB4 cells for AFM indentation measurements. The photo resistant material was patterned using soft lithography and the

dimensions of the microwells were optimized to confine suspended cells while maintaining them within a reachable range of the AFM probe.

1.3 Framework

All experimental factors such as applied forces, force curve resolutions and loading rates, that can largely influence the determination of the elasticity values, were carefully considered and optimized in the data collection and fitting process (Chapter 2). The development of an automated batch analysis code provides the possibility to fully understand the fitting models and obtain fast and consistent comparisons. It also permits to identify the appropriate criteria for cancer cell measurements. Such criteria include proper contact point location determination and identification of the maximum indentation length that should be fitted to avoid any substrate effect. Optimization process can be found in Chapter 3, Section Chapter 3.

NB4 cells were then treated using ATO to monitor induced cell elasticity changes using AFM based force indentation measurements, and to correlate the cancer cell mechanics to viability and cell morphology. Results are presented in Chapter 3 (Section 3.2). Providing such relations may find itself to become a powerful tool for cell identification and drug screening. In summary, the systematic procedures described in this Thesis will provide practical guidelines for researchers interested in quantifying cell elasticity[70,71]. They have also been exploited in order to collect AFM indentation measurements and conduct viability tests on drug treated leukemia cells.

CHAPTER 2: MATERIALS AND METHODS

2.1 Cell Culture

The NB4 cell line, derived from human promyelocytic leukemia, was provided from Mount Sinai Hospital in Toronto (Dr. Chen Wang). The cells were ordered from DSMZ (Deutsche Sammlung von Mikroorganismen Zellkulturen, Brauschweig, Germany. Catalogue #: ACC-207). NB4 cells were cultured in Gibco® DMEM (Life Technologies, NY, USA), high glucose, with 10% of Gibco® heat-inactivated fetal calf serum (Life Technologies, NY, USA) and 1X of Gibco® Penicillin (Life Technologies, NY, USA) in a humidified incubator (Sanyo North America Corp., IL, USA) containing 5% CO_2, 95% humidity at 37°C. Cells were passaged every 2-3 days to maintain a cell population of 10^5 cells/mL within 75 cm^2 Corning™ Biocoat™ cell culture flasks (Fischer Scientific, PA, USA).

2.2 Drug Treatment

For the viability and AFM experiments on NB4 cells and drug treated NB4, 10 mL cell solution of 10^5 cells/mL was aliquot in multiple 25 cm^2 cell culture flasks (Fisher Scientific, PA, USA), in order to compare treated cells with the same original population. Then each flask of NB4 cells was treated with a single dose of ATO (Sigma-Aldrich, WI, USA) solution prepared in Gibco® PBS of pH 7.4, without calcium or magnesium (Life Technologies, NY, USA). Viability experiments were repeated 6 times using ATO concentrations of 0, 5, 10, 20 and 30 μM. Following viability testing, AFM experiments were performed over 48 h using a 30 μM ATO treatment only.

2.3 Viability Assays

2.3.1 Trypan Blue Staining

Using Trypan Blue (Sigma-Aldrich, WI, USA) staining the amount of live and dead cells within a sample was counted over a hemocytometer. A dilution factor of 1:1 in volume (Trypan Blue: cell solution) was used for 1 mL of the solution. A blank cell solution was used as a negative control; and a 10 mL cell solution was treated with 10 µL of PBS and used as a positive control. Cell solutions treated with 3, 10, 20 and 30 µM ATO were monitored, respectively. Viability measurements were calculated using the following equation for stained and unstained cells for each assessed time after treatments:

$$\%\, Viability = \frac{live\ or\ unstained\ cell\ count}{Total\ cell\ count} \qquad \text{Eq. 1;}$$

Average viabilities were measured over five different grids (1 mm x 1 mm) of the hemocytometer. 6 different cell volumes were assessed, in order to measure the average cell viability for each monitored time after treatment. These gave a quick overview of the drug effects on NB4 cells within 48 h. An automated cell counter seemed to be a viable instrument to collect a sufficient amount of measurements, but unfortunately > 10% error was found for tests with lower than 50% viability depending on different parameter settings. As it is necessary to measure small variability in this study, an alternate solution was required.

2.3.2 Microplate Fluorescence Readings

FLUOstar Omega microplate reader (BMG Labtech, ON, Canada) was used for all microplate fluorescence readings experiments, together with the LIVE/DEAD® Viability/Cytotoxicity Kit for Mammalian Cells (Life Technologies, NY, USA). The Kit contains

both ethidium-1 (EthD-1) and calcein AM stock solutions. 15 µL of the 2 mM EthD-1 stock solution was added to 10 mL of sterile tissue culture-grade PBS. Subsequent to mixing using a vortexer (VWR Scientific, PA, USA), 4 µL of the 4 mM calcein AM stock solution was added to the PBS and EthD-1 solution, and further vortexed to finalize the labelling solution.

The microplate reader utilizes a Xenon flashlamp allowing spectral readings between 240 and 800 nm for 8 different integrated excitation and emission filters. As excitation and emission wavelengths of calcein AM are of around 494 nm and 517 nm, respectively, live cell populations were recorded using the recommended standard FITC filter (465 to 556 nm). EthD-1 on the other hand is excited at around 528 nm and emits fluorescence at around 617 nm in the presence of DNA. Thus a Texas Red filter of wavelength range between 540 and 648 nm was chosen for the detection of dead cells.

In order to remove most of the background fluorescence from FBS and DMEM solutions, measurements were done in PBS solution. Treated cell solutions were centrifuged at 800 rpm for 5 min and supernatant was aspirated. Cells were resuspended in warm 1X PBS, and repeated the centrifugation and supernatant removal. Finally, the NB4 cells were resuspended in warm 1X PBS.

100 µL of the cell solution in PBS was placed in each well of the 96-well plate (Fischer Scientific, ON, Canada). An equal volume of 100 µL labelling solution was then added to each microplate well. The 96-well plate was kept in the 37°C incubator for 25 min before any reading experiments. For each assessed sample, fluorescence intensity readings from 48 respective microplate wells were collected using the specified filters. The adjustable gain was set at 10% in order to effectively record larger intensity readings at early (large amount of live cells) and later (large amount of dead cells) stages of the treatments. The background intensity value was

averaged from 16 microplate wells containing 100 µL of PBS mixed with 100 µL of labelling solution. Live and dead cell populations were assessed simultaneously for each microplate within the microplate reader.

It is important to note that these fluorescence viability assays do not provide information on the absolute total cell population but only the relative population from one sample to another. As these measurements are population dependent, a batch of cells was aliquot before treatment and measurement. Relative live and dead cell populations were measured and calculated by comparing them to the largest and smallest fluorescence intensity readings from the adequate filters. 48 microplate wells containing 100 µL of cell solution each were assessed for the monitored time point. These involve not only more measurement values than when performing Trypan Blue staining assays, but also larger sampling offering statistically meaningful data. The smallest fluorescence intensity reading for calcein AM with an emission wavelength of 535 nm was associated to a relative live cell population of 0%, meanwhile the largest reading recorded was associated to a population of live cells only (100%). Same rules applied in the calculation of relative dead cell populations by recording the emission wavelength of EthD-1 at 620 nm. The positive control (PBS treated cell solution) was used to record the average background measured by the instrument, which was subtracted from each measurement value. Equations for live (535 nm filter) and dead (620 nm filter) cell population were the following:

$$\%\ live\ cells = \frac{\left(I_{sample}^{535} - I_{bgd}^{535}\right) - \left(I_{min}^{535} - I_{bgd}^{535}\right)}{\left(I_{max}^{535} - I_{bgd}^{535}\right) - \left(I_{min}^{535} - I_{bgd}^{535}\right)} \qquad \text{Eq. 2;}$$

$$\%\ dead\ cells = \frac{\left(I_{sample}^{620} - I_{bgd}^{620}\right) - \left(I_{min}^{620} - I_{bgd}^{620}\right)}{\left(I_{max}^{620} - I_{bgd}^{620}\right) - \left(I_{min}^{620} - I_{bgd}^{620}\right)} \qquad \text{Eq. 3;}$$

where I represents the measured fluorescence intensity reading and superscripts 535 and 620 represent emission wavelength for the calcein AM (live/green, 535 nm) and EthD-1 (dead/red, 620 nm). Additional indexes in subscript ($sample$, max, min and bgd) characterize the readings for the sample, maximum, minimum and background intensity readings in that order.

2.4 Morphology Assessment

Morphology alterations were monitored both quantitatively and qualitatively. Quantitative evaluation of cell size was performed by measuring the ratios of cell diameter to microwell diameter as SU8-10 microwell diameters were defined during substrate fabrication and verified using a non-contact profilometer. For untreated NB4 cells, the estimation of cell diameters could thus be carried out. However, as the cell shapes were found to become more and more irregular after treatment, a qualitative inspection of cell morphology was required. Qualitative inspection was done by describing overall cell shapes at different times after treatment. Upon visual inspection, characteristic morphology changes, such as shrinking, blebbing and fragmentation, could be linked to different apoptosis stages previously discussed in the introduction.

2.5 Preparation of Microwells

Figure 3 displays the step-by-step procedure to fabricate an SU8-10 microwell array substrate to mechanically confine APL cells. #1 glass coverslips were first cleaned in Piranha solution (mixture of 1:4 of 30% H_2O_2 and 96% H_2SO_4), thoroughly rinsed with 18 MΩ·cm Milli-Q H_2O and finally dried in a nitrogen stream. (*Caution: Piranha solution is a strong oxidant,*

reacts violently with organic materials and should be handled with outmost care). A clean coverslip was fixed in the spin coater (Laurell Technologies Corporation, PA, USA) before depositing 5 drops of SU8-10 photoresist solution (MicroChem, MA, USA). Spin coating at 3000 rpm for 65 s was performed according to the manufacturer's protocol to control microwell depth between 6 to 8 µm. Microwell depth was confirmed using a cyberSCAN CT 100 high resolution non-contact profilometer (Cyber Technologies, Eching-Dietersheim, Germany) (Figure 4).

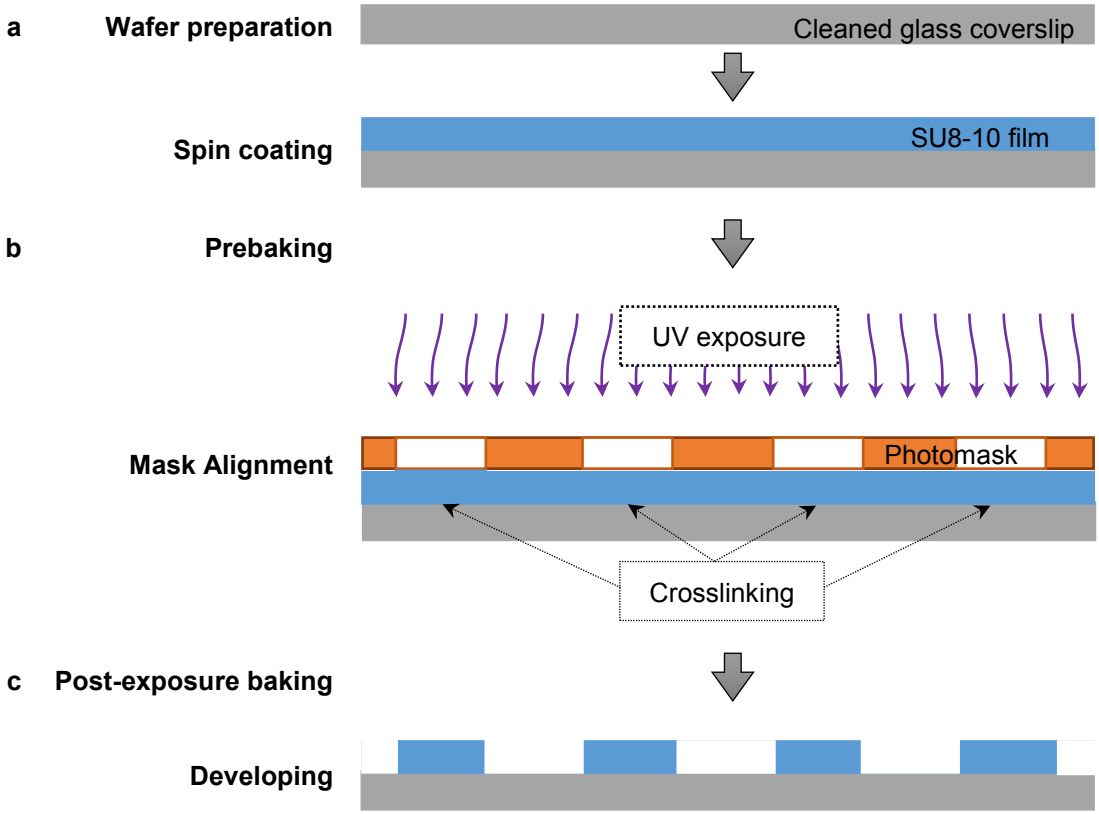

Figure 3. SU8-10 microwell arrays fabricated on glass coverslips by soft lithography technique. SU8-10 was spin coated on cleaned glass coverslip to obtain a uniform film (a). After prebaking the SU8-10 film was patterned using a photomask with an array of 20 µm circles inside the mask aligner undergoing UV exposure (b). After the post-exposure baking the non-crosslinked SU8-10 film areas were removed from the glass coverslip *via* immersion in the developer solution to generate an SU8-10 microwell array (c).

Once the final spin coating procedure terminated, substrates were baked using heat blocks at 65°C for 2 min followed by further baking at 95°C for 5 min to evaporate the coating solvent and densify the coating after spin coating, respectively. The substrate was then placed in the mask aligner (Karl Suss America Inc., VT, USA) against a photomask (HTA Photomask, CA, USA) patterned by an array of 20 μm circles. Both the substrate and photomask were exposed to UV light for 12 s. Longer exposure time may result in backscattering and decompose development inhibitors away from the exposed film areas within the patterned circles. This may explain the sloping of the microwell walls seen in Figure 4b of ± 1 μm. Substrates were then post-exposure baked for 1 min at 65°C and 2 min at 95°C in order to remove standing wave ridges by diffusing the photoactive compound in the resist.

Finally, the SU8-10 film on the coverslip (in short SU8-10 substrate) was left untouched overnight before immersion into the SU8 developer solution of 1-methoxy-2-propanol acetate (MicroChem, MA, USA) for 2 min, mixing gently every few seconds. Substrates were then rinsed with isopropanol and dried using a nitrogen stream, followed by a baking at 35°C for 1 to 2 h to harden the final SU8-10 film before final inspection. No major or minor cracks should be observed in the film by optical microscopy.

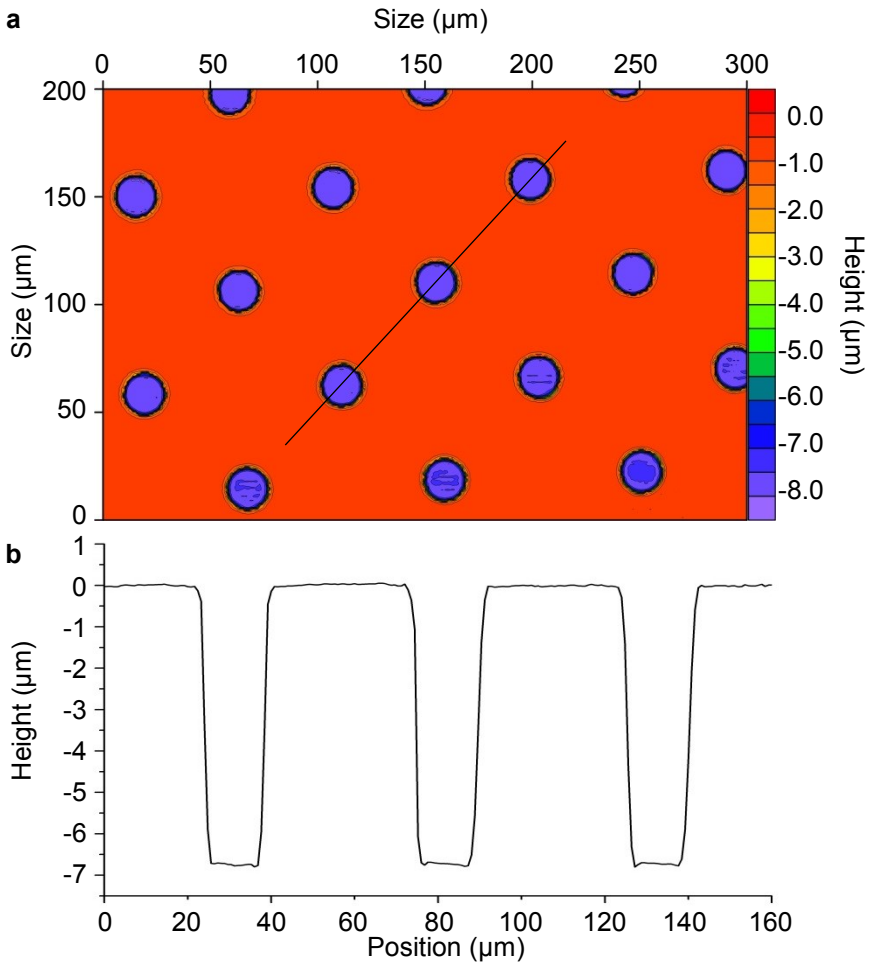

Figure 4. Non-contact profilometer image of the SU8-10 microwells (a) and the height profile of the microwells (b).

2.6 AFM Measurements

Both the SU8-10 microwell substrate and AFM liquid cell were thoroughly rinsed using 70% ethanol and 18 MΩ·cm Milli-Q H_2O consecutively. The SU8-10 substrate was then placed at the bottom of a closed liquid cell (JPK Instruments CoverslipHolder (JPK Instruments, Berlin, Germany), which was successively filled with 800 μL of DMEM with 1X penicillin before placing it into a vacuum chamber. After vacuuming for 30 min, no air bubbles should be visible. It should be noted that no fetal bovine serum was used due to its viscosity which would cause

formation of foam during vacuuming. The DMEM and penicillin solution was systematically replaced with 200 μL of warm culturing media at 37°C, followed by the addition of 100 μL of cell solution in the liquid cell. The whole sample was placed on the AFM stage for 10 min before any further testing, to ensure the NB4 cells settled inside the microwells. This is to ensure that isolated single NB4 cells can be located in the SU8-10 microwells and probed by AFM. For the later post-treatment times, small amount of cells were left in the samples. Therefore, a total of 200 μL of cell solution was used for AFM indentation measurements.

Force-indentation curves were collected using a JPK Nanowizard® II BioAFM (JPK Instruments, Berlin, Germany) setup mounted on an inverted microscope (1X81, Olympus, Japan) with a manual precision stage (JPK Instruments, Berlin, Germany), under force mapping mode. Contact mode conical probes (DNP-10, Bruker AFM Probes, CA, USA) with nominal spring constant of 0.06 N/m and colloidal probes (sQube®, Wetzlar, Germany) with nominal cantilever spring constant of 0.08 N/m were used for the analysis of the conical (Eq. 8) and the spherical models (Eq. 9). Spring constants of each cantilever were individually determined by using the thermal noise method[72,73]. The spring constants were measured in the 0.068-0.102 N/m range for conical and 0.047-0.071 N/m range for spherical probes, respectively.

Figure 5 displays the schematic AFM setup for cell indentation measurements. The spherical probe attached to the AFM soft cantilever was used to indent the confined APL cells (pink). As shown, cell immobilization was achieved by using the fabricated patterned SU8-10 substrate, which was displayed as a bright field image on the top right of Figure 5. The 20 μm microwells were sized to restrain the 15 μm cells. The 6 to 8 μm depth of the microwells facilitate cell indentation by stably localizing cells inside the microwells while maintaining a portion of the cell above the flat SU8-10 film surface.

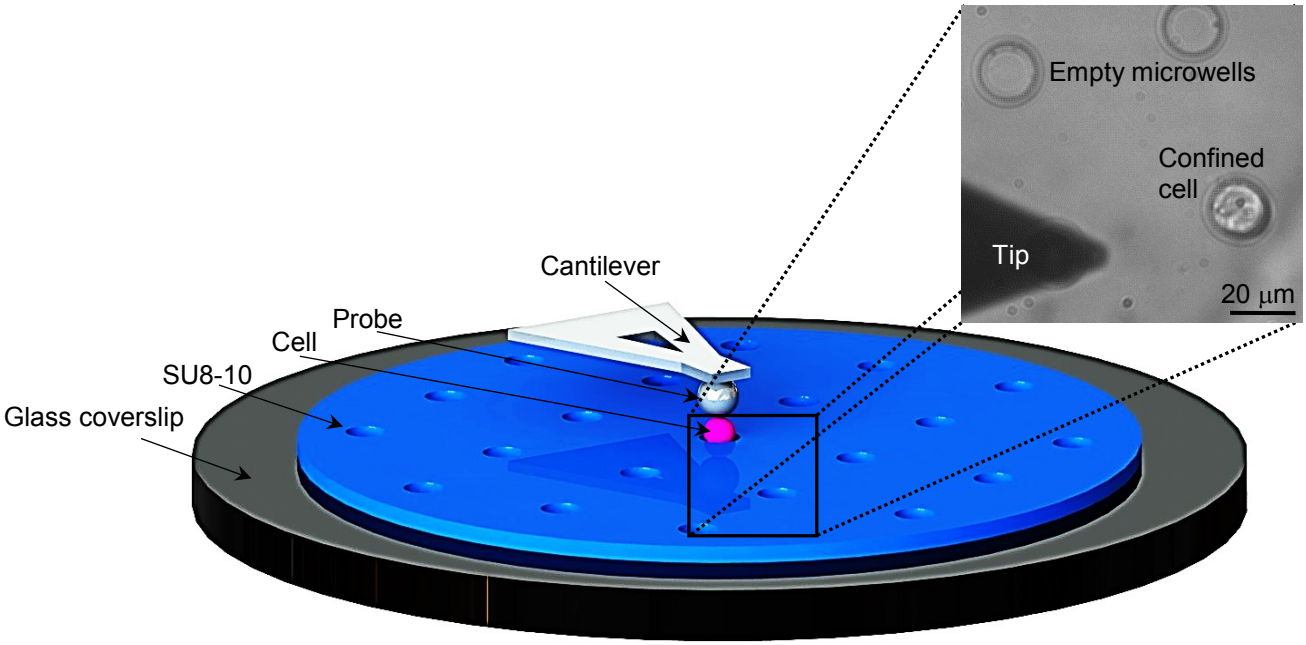

Figure 5. Main components of the experimental AFM setup to probe a single NB4 cell (pink) using a spherical tip (gray). Cell is confined within the patterned SU8-10 film microwell (blue) prepared over a glass coverslip wafer (black). A top view optical bright field image (top right) of the SU8-10 microwell array displaying empty microwells, a confined NB4 cell within a microwell as well as the AFM tip.

Arrays of curves (vertical deflection versus *z*-piezo displacement) were collected over multiple ($10<n<15$) NB4 cells with selected grid sizes of 7 by 7, 15 by 15, 25 by 25, and 64 by 64 grids. Scan size was limited to 10 nm by 10 nm, in order to restrict lateral movement of the cantilever and constrain the probe motion above the cell surface. The procedure was repeated using both the conical and spherical probes. Only the approaching force curves collected for each grid were analyzed. A constant loading rate of 2 μm/s and a maximum load ranging from 0.5 to 2.0 nN were applied[7]. From the cantilever spring constants and applied load range, the maximum deflection of the cantilever was between approximately 10 nm and 30 nm. The sampling rate was set to 2047 Hz in order to obtain over 3000 data points per curve for a *z*-scan length of 3 μm

(maximum *z*-scan range is 15 μm). Extending and retracting delays were used (total of 0.2 s) to allow the NB4 cells to relax between consecutive indentations.

15 sets of deflection-displacement curves (49/225/625/4096 curves per set) were batch analyzed using a self-developed code implemented in IGOR Pro 6 (Wavemetrics, OR, USA). For each curve, the Young's modulus was extracted using respective equations and models (*vide infra*).

2.7 Fitting Models

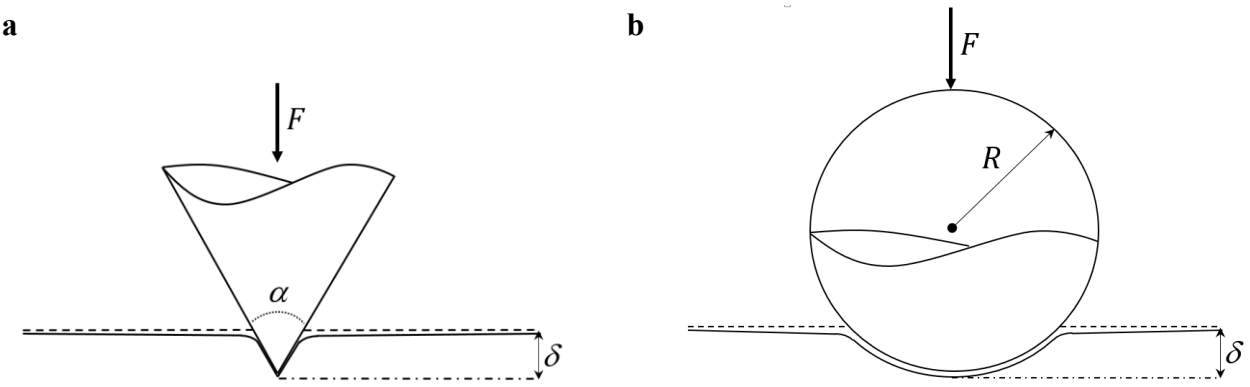

Figure 6. Contact mechanics model of a conical indenter (a) and a spherical indenter (b) both indenting an elastic half-space.

Conical: $$F = \frac{2E \tan\alpha\, \delta^2}{\pi(1-\nu^2)}$$ Eq. 4;

Spherical: $$F = \frac{4E\sqrt{R}\delta^{3/2}}{3(1-\nu^2)}$$ Eq. 5;

Two models using spherical and conical contact mechanics models were considered (Figure 6). Although models are often popularly referred to using force (F) versus indentation (δ) curves as seen in Eq. 4 and Eq. 5 in order to calculate the Young's modulus (E), they are actually

derived from the cantilever deflection (d) as a function of the ramp of the z-piezo (Z) and the cantilever's spring constant (k). Thus, by substituting Eq. 6 and Eq. 7 in Eq. 4 and Eq. 5, one can obtain Eq. 8 and Eq. 9[68,74-76]. Each data point, i, of a deflection-displacement curve can be defined as (Z_i, d_i) and the contact point being labeled by the index 0 (Z_0, d_0). Indentation process and fitted force curve are observed in Figure 7.

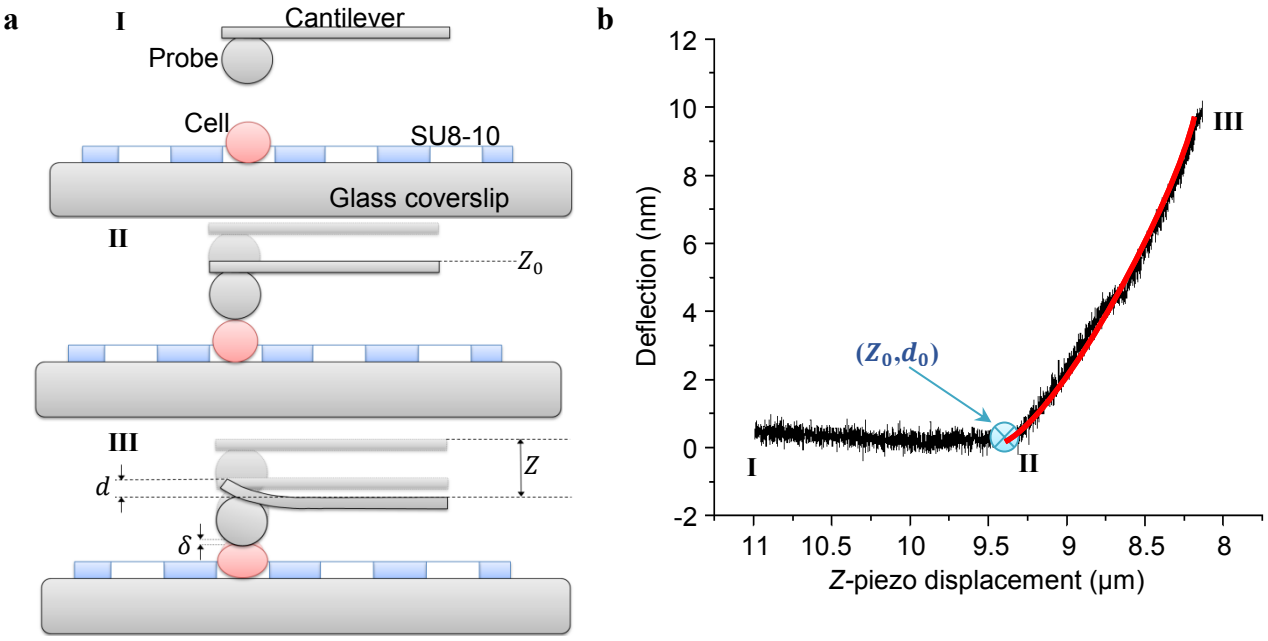

Figure 7. Indentation process of a single cell using AFM (a), and force curve with a fit to Eq. 9 (b). Probe is 1.5 to 2 µm away from the cell (I), then probe is in contact with the cell, defining the contact point (Z_0, d_0) (II) and indented for the defined scan length (III).

Theoretically, the Young's modulus is a constant value which describes the elastic behavior of solid materials, such as polymers, when submitted to stress. However, in reality, cells harden upon indentation. The same predicament can be observed when assuming a Poisson's ratio value for cells, another parameter describing the elastic behavior of isotropic materials. However, current literature has used contact mechanics models to simplify data

analysis and has made use of these models for comparability purposes. These models were used in order to compare the measured Young's modulus to available literature[69,77,78].

The Poisson's ratio (v) was set to 0.5, as the material is assumed to be perfectly incompressible in order to simplify the model[79-82]. In both models, information on the probe size and geometry is required, namely the opening angle (α) when using a conical probe and the radius (R) when using the spherical model.

$$F = kd = k(z - \delta) \quad \text{Eq. 6;}$$

$$\delta = (Z - Z_0) - (d - d_0) \quad \text{Eq. 7;}$$

In order to simplify the data processing and use only one fitting model, all data were processed two times, using first the deflection versus ramp size curves, fit to Eq. 8 and Eq. 9, and then the force-indentation curve, fit to Eq. 4 and Eq. 5, for comparison purposes and validation[83].

Conical model:

$$Z = Z_0 + (d - d_0) + \left[\frac{\pi k(d - d_0)(1 - v^2)}{2E \tan \alpha}\right]^a \quad \text{Eq. 8;}$$

where $a = {}^1/_2$

Spherical model:

$$Z = Z_0 + (d - d_0) + \left[\frac{3k(d - d_0)(1 - v^2)}{4E\sqrt{R}}\right]^a \quad \text{Eq. 9;}$$

where $a = {}^2/_3$

2.8 Automated Data Processing Code

One of the challenges encountered during force data processing was to accurately fit over 50,000 curves using self-defined criteria within a reasonable timeframe. An automated data processing code was thus necessary to enable the handling of large data sets comprising different

formats including commercial AFM and ACSII files. The code also needed to include an extensive range of capabilities for scientific analysis such as the creation of user-defined curve fitting approaches and plotting of processed data.

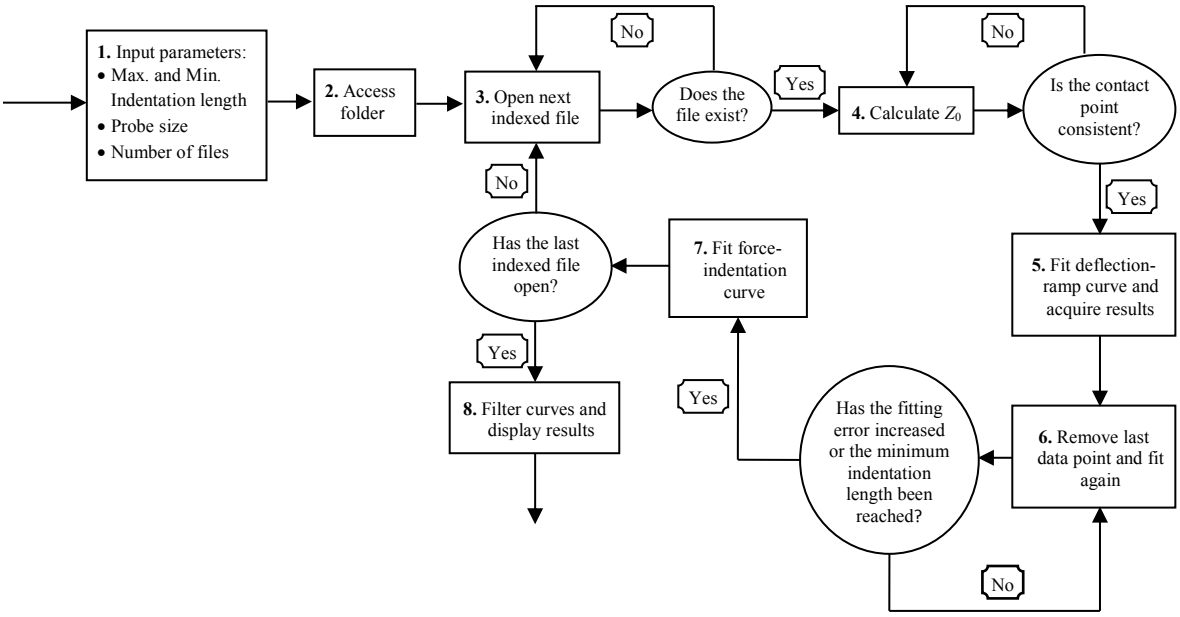

Figure 8. The design of the analysis code processing steps, including the input of fitting parameters (1), accessing folder (2), opening indexed file (3), calculating the contact point (4), fitting the deflection-ramp curve (5) minimizing the fitting error (6), fitting the force-indentation curve (7), and filtering and displaying results (8).

As illustrated in Figure 8, the first step requires the user to indicate specific physical and geometrical parameters (*i.e.,* spring constant (k), Poisson's ratio (v) and probe size (R or α)) in addition to other variables such as the number of force curves, the folder path location and the file name. Once launched, the first indexed ASCII file (or curve) retrieved from a specific folder (step 2) is opened: the deflection and ramp waves of a single force curve are now loaded (Figure 8, step 3). Successively, an initial approximation of the contact point location is set according to the profile of the curve (*i.e.*, close to the non-linear portion). Based on Eq. 8 and Eq. 9, the calculations of the Z_0 are repeated until the location values from consecutive processes remain

the same. The corresponding d_0 should now be offset to zero (Figure 8, step 4). The following step is to fit the deflection-ramp curve once using the maximum or portion of the indentation length (Figure 8, step 5), a parameter provided by the user using the least squares method. The curve is fit again by deleting the last data point, and the code will stop processing until the fitting error does not increase or the minimum indentation length is reached (Figure 8, step 6). The fitting information and fit results such as the Young's modulus (calculated by using both a deflection-ramp curve and a force-indentation curve), fitting errors, number of fitted data points and contact point location, as well as the specific curve numbers is recorded and tracked (*i.e.*, each deflection curve is numbered and fitting information for each of them is linked to that number). From this accessible fitting information, specific fitting criteria were defined, such as the reference points that should be used to locate the contact point. Furthermore, the force-indentation curve is also fit as additional evidence of the data compliance with the model (Figure 8, step 7). Finally, the code returns to step 3 and repeats the procedure using the next indexed file.

When collecting a force map with the AFM, a force set folder is saved including the indexed deflection-ramp distance curves as text files. Thus, when the code consecutively investigates each text file, it stops once the last indexed file within a recorded force set is processed. When the fitting criteria are not met some of the curves including no tip-sample contact, incomplete curves (*i.e.*, with smaller scan lengths or applied forces than the experimental settings), and curves with an insufficient amount of data points can be filtered by the code. This option enables fast analysis of the average fitting information (see Batch Analysis Code Performance section for further details). It can also plot histograms to observe the full data set and their variability (Figure 8, step 8).

The automated batch analysis algorithm has a unique looping protocol for Young's modulus extraction from individual curves as it thoroughly analyzes each one of them and focuses on the importance of systematic assessment and not on average results. Programming was also created to be user-friendly. In particular, users are assisted step by step throughout their fitting process.

2.8.1 Batch Analysis Code Performance

2.8.1.1 Code Options

In order to automatically process a large number of force curves, the analysis code was developed involving different fitting options (*vide supra*), such as contact point criteria, the use of the spherical or conical model to fit either the approaching or retracting force curves, as well as manual parameter inputs such as the Poisson's ratio and spring constant. These options are fully controllable and functional for comparing the fitting results.

The first option in the code is to manually change the fitting parameters such as the Poisson's ratio (υ), spherical probe radius (R) or conical probe opening angle (α) and spring constant (k) of the cantilever. Easy access to these parameters helps in identifying the impact of each of these parameters on the fitting themselves. Additionally, it is possible to observe the fit curve overlaying the raw data if required by the user. This is often considered and needed when the calculated fitting errors are larger than expected for some particular curves. It allows a quick overview of the force curve batch as the fittings are performed. Of course, both conical and spherical fitting models were introduced in the batch analysis code to compare the variability of the data and elasticity measurements using either of them.

Code options involve the choice of using either the retracting or the approaching force curve for the fitting. The curve itself can also be fit within an indentation range which may be specified by the user. By selecting different minimum and maximum indentation length to fit the force curves, it is possible to determine the softer and harder indentation regimes of a deflection curve.

As deflection-displacement measurements are performed within a dynamic system, curves must be tracked thoroughly to avoid measuring neighboring cell motion, or cantilever resonance. In order to efficiently assess the affected force curves, specific filtering criteria are required. For fast analysis purposes and to obtain a meaningful value for the average data output, force curves can also be filtered to identify outliers which often include force curves that are inconsistent with the fitting model. The most accurate way to identify these curves is to compare the Young's modulus given by the deflection-*z*-piezo displacement curve with the one extracted from the force-indentation curve. Ideal curves that comply with the model promise to generate the same Young's modulus values using either model. This criterion was chosen as it applies to any sample and fitting model used, meanwhile fitting errors can vary according to the number of data points within a force curve.

Moreover, consistency in identifying the contact point of the deflection *vs.* *z*-piezo displacement curves using two data points (Z_1, d_1) and (Z_2, d_2) for calculation was found to be a good indicator for sorting the curves. In the case of APL-NB4 cells, curves that have a contact point differing of over 500 nm when calculated using different (Z_1, d_1) and (Z_2, d_2) reference points should be considered as outliers. Finally, curves that were missing a baseline to properly measure the contact point were considered to not conform to the fitting models and were filtered out.

In addition, the code is also compatible with different text file layouts as different AFM instruments export the data curve in different formats. Thus, as both the JPK and DI (Bruker) software were available, the batch analysis code can be used for either formatting type. This is important to consider for users performing experiments on different AFM instruments. The code's script can be found in Appendix A.

2.8.1.2 Batch Analysis Efficiency

As manually fitting a force curve may take over 10 min when calculating and recalculating the contact point before extracting the Young's modulus, a fast and reliable batch analysis code was required. Data collection time alone is dependent on AFM parameters used, such as the force map grid size, sample rate, and delays (or dwell time) of approach and retract.

Table 1. Time efficiency of the batch analysis code.

Force map grid size	**7 x 7, n=49**	**15 x 15, n=225**	**25 x 25, n = 625**	**64 x 64, n=4096**
Exporting Map to ACSII file time (h:min:s)	~ 0:0:45	~ 0:0:45	~ 0:0:45	~ 0:0:45
File loading time (h:min:s)	~ 0:0:50	~ 0:0:50	~ 0:0:50	~ 0:0:50
Fitting time (h:min:s)	~ 0:0:16	~ 0:1:15	~ 0:3:47	~ 0:55:36
Total time (h:min:s)	~ 0:1:51	~ 0:2:50	~ 0:5:22	~ 0:57:11

*Sample rate : 2047 Hz

Table 1 shows the time efficiency of the batch analysis code for different force map grids evaluated using a 2.40 Hz processor. Time required exporting the collected force map as ACSII files and loading them in the IGOR Pro software are mostly dependent on the speed of users.

However, fitting time is related to the number of curves to be fit. Hence, data processing is more efficient when a greater number of curves, n, is processed. Unfortunately, the code may only fit a single force map at a time. Thus, between each force map, file path must be located and the specified fitting model and its parameters must be selected before loading the curves. These aspects will be part of further improvement of the code itself.

CHAPTER 3: RESULTS AND DISCUSSION

3.1 AFM Force Indentation Analysis

3.1.1 Optimization of the Contact Point Location Calculations

The accuracy of the contact point location (Z_0, d_0) will influence the fitting and thus the resulting Young's modulus. In order to achieve the optimal fitting to the selected models and extract comparable Young's modulus values, one of the first steps in the automated processing is to identify the location of the contact point (Z_0, d_0).

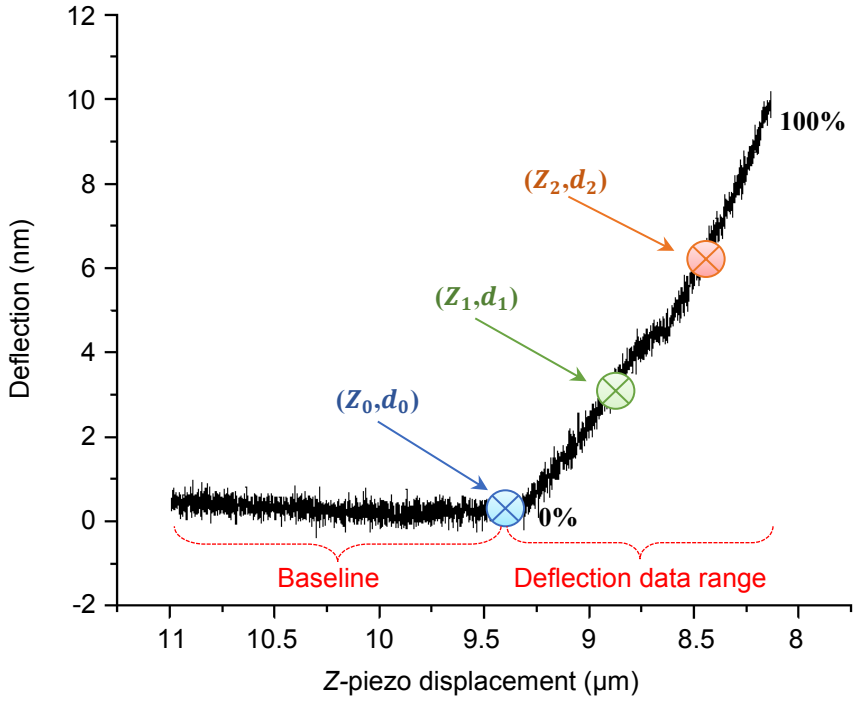

Figure 9. Reference points (Z_1, d_1) and (Z_2, d_2) located between 0% and 100% of the defection, used to determine the contact point (Z_0, d_0) on an experimentally captured deflection-displacement curve.

As shown in Figure 9, two reference points, (Z_1, d_1) and (Z_2, d_2) are selected on the deflection curve. (Z_1, d_1) is chosen in order to best represent the cell behavior upon small deflection, *i.e.*, closer to 0% of the deflection, meanwhile (Z_2, d_2) represents the larger deflection

portion, *i.e.*, closer to 100% of the deflection. Noteworthy, it should be emphasized that neither point is chosen within the baseline region, which should not be fit as it does not represent any contact between the tip and sample. When offsetting the deflection to the point at which the probe and cell were in contact ($d_0 = 0$), the contact point finding Eq. 10 became[83]:

$$Z_0 = \frac{(Z_2 - d_2) - (Z_1 - d_1)\left({}^{d_2}/_{d_1}\right)^a}{1 - \left({}^{d_2}/_{d_1}\right)^a} \qquad \text{Eq. 10;}$$

where $a = {}^1/_2$ (conical) or $a = {}^2/_3$ (spherical).

By systematically offsetting the deflection d_0 to zero, the contact point can be recalculated until its location remains constant or within a given range (*e.g.*, 0 to 25 nm). Figure 9 represents an experimental deflection-displacement curve for which a maximum applied force of about 0.5 nN was used (the cantilever spring constant was 0.059 N/m). This gave the maximum deflection of the cantilever to approximately 10 nm. The *z*-piezo displacement length was set to 3 μm (measured between 11 and 8 μm in Figure 9, within the total *z*-scan range of 15 μm).

In principle, for an ideal curve where the relation between deflection (or force) and displacement (or indentation) perfectly matches the model, regardless of which two points (Z_1, d_1) and (Z_2, d_2) are selected, it would result in the same contact point location. In reality, with different noise levels and non-ideal correlations, the contact point may vary when choosing different (Z_1, d_1) and (Z_2, d_2). Thus, how to select the location of (Z_1, d_1) and (Z_2, d_2) is critical for determining the contact point location. Here, systematic paring comparisons were evaluated by selecting these points based on the percentage of the deflection, setting the largest deflection

at 100%, and the baseline of deflection at 0%. The analyzed results are shown in Table 2 and Table 3.

Table 2. Fitting analysis results for 49 force curves extracted consecutively using 0.5, 1.0 and 2.0 nN applied forces. Different reference points (Z_1, d_1) and (Z_2, d_2) were chosen.

Force (nN)	(Z_1, d_1) (% curve)	(Z_2, d_2) (% curve)	Average Fitting error (nm ± SD)	Average indentation length (nm ± SD)	Average number of data points (± SD)	Average Z_0 location (nm ± SD)
0.5	10	25	527.7 ± 204.0	1127.3 ± 379.2	1539.9 ± 558.3	-8012.8 ± 607.1
		50	477.3 ± 162.8	1011.7 ± 246.9	1367.5 ± 343.0	-7910.3 ± 527.0
		60	**454.8 ± 150.9**	**998.5 ± 257.8**	**1349.9 ± 360.2**	**-7897.2 ± 515.1**
		75	442.8 ± 148.9	973.4 ± 259.3	1314.9 ± 361.2	-7872.0 ± 511.0
		90	431.8 ± 140.3	955.5 ± 237.6	1288.8 ± 327.5	-7854.1 ± 501.8
	15	25	497.5 ± 230.8	1102.7 ± 397.4	1508.9 ± 593.9	-7963.2 ± 607.5
		50	449.5 ± 163.7	989.3 ± 271.1	1337.1 ± 378.6	-7887.9 ± 523.6
		60	429.9 ± 151.1	975.5 ± 267.9	1318.8 ± 376.5	-7874.1 ± 492.2
		75	418.7 ± 157.5	934.6 ± 267.5	1261.3 ± 373.1	-7833.0 ± 499.6
		90	404.3 ± 143.0	909.5 ± 243.6	1225.3 ± 335.8	-7808.0 ± 500.0
1.0	10	25	508.6 ± 207.1	1067.3 ± 372.9	1496.6 ± 548.6	-5424.7 ± 796.8
		50	432.8 ± 169.7	913.1 ± 286.6	1265.6 ± 379.7	-5269.9 ± 816.8
		60	412.0 ± 164.8	893.8 ± 290.3	1237.8 ± 382.3	-5250.6 ± 832.1
		75	390.9 ± 167.0	858.0 ± 282.0	1184.4 ± 353.5	-5214.7 ± 852.3
		90	390.5 ± 178.0	864.7 ± 304.0	1194.2 ± 387.1	-5221.4 ± 874.5
	15	25	472.4 ± 197.5	992.1 ± 350.3	1384.1 ± 497.8	-5349.2 ± 815.4
		50	405.4 ± 180.9	885.5 ± 315.2	1224.4 ± 406.8	-5242.2 ± 862.2
		60	372.0 ± 180.9	841.9 ± 311.6	1162.3 ± 401.4	-5198.4 ± 877.3
		75	369.1 ± 188.1	824.3 ± 314.9	1136.8 ± 402.2	-5180.6 ± 879.2
		90	174.5 ± 70.0	819.2 ± 332.0	1128.7 ± 420.5	-5175.5 ± 907.5
2.0	10	25	443.8 ± 127.8	935.7 ± 226.8	1337.0 ± 336.9	-5191.1 ± 390.4
		50	416.9 ± 86.2	889.9 ± 143.1	1268.2 ± 199.4	-5145.1 ± 357.9
		60	409.8 ± 83.3	884.5 ± 135.7	1260.4 ± 189.0	-5139.6 ± 354.4
		75	401.6 ± 77.7	871.8 ± 133.6	1242.1 ± 185.7	-5126.8 ± 358.2
		90	396.2 ± 68.5	870.1 ± 126.7	1239.6 ± 175.3	-5125.1 ± 347.7
	15	25	431.3 ± 113.9	903.9 ± 172.5	1288.0 ± 239.4	-5159.0 ± 383.1
		50	406.8 ± 94.5	875.4 ± 149.8	1246.4 ± 203.3	-5130.3 ± 362.9
		60	399.3 ± 88.5	872.6 ± 140.0	1242.4 ± 188.5	-5127.6 ± 356.3
		75	392.9 ± 77.5	861.6 ± 132.9	1226.7 ± 179.5	-5116.4 ± 352.1
		90	385.4 ± 71.2	855.4 ± 129.5	1217.9 ± 175.8	-5110.2 ± 348.2

Before selecting the two points, some general rules should be applied: (1) (Z_1, d_1) should not be located below 10%, in order for the code to have enough data points (prior to the contact point) to separate the baseline data points from the deflected data points; (2) (Z_2, d_2) should not be selected below 50%, in order to avoid representing only the shallow indentation portion of the deflection-displacement curve which may cause Eq. 10 to misinterpret the location of the contact point; (3) when selecting (Z_1, d_1) to be above 20% of the deflection, the lower deflection regime is not fully taken into account in the contact point Eq. 10 and may cause a misapprehension of the contact point location. Therefore, (Z_1, d_1) should be selected between 10 and 20%.

Table 3. Fitting analysis results for 49 force curves extracted consecutively using a 0.5 nN applied force. Different reference points (Z_1, d_1) and (Z_2, d_2) were chosen. All results are compared to the reference at which (Z_1, d_1) and (Z_2, d_2) are set at 10% and 60%, respectively.

(Z_1, d_1) (% curve)	(Z_2, d_2) (% curve)	Average variation ratio of the fitting error* (± SD ratio)	Average variation ratio of the indentation length* (± SD ratio)	Average variation ratio of the number of data points* (± SD ratio)	Average variation ratio of the Z_0 location* (nm ± SD ratio)
	25	1.16 ± 1.35	1.13 ± 1.47	1.14 ± 1.55	1.01 ± 1.18
	50	1.05 ± 1.08	1.01 ± 0.96	1.01 ± 0.95	1.00 ± 1.02
10	**60**	**1.00 ± 1.00**	**1.00 ± 1.00**	**1.00 ± 1.00**	**1.00 ± 1.00**
	75	0.97 ± 0.99	0.97 ± 1.01	0.97 ± 1.00	1.00 ± 0.99
	90	0.95 ± 0.93	0.96 ± 0.92	0.95 ± 0.91	0.99 ± 0.97
	25	1.09 ± 1.53	1.10 ± 1.54	1.12 ± 1.65	1.01 ± 1.18
	50	0.99 ± 1.08	0.99 ± 1.05	0.99 ± 1.05	1.00 ± 1.02
15	60	0.95 ± 1.00	0.98 ± 1.04	0.98 ± 1.05	1.00 ± 0.96
	75	0.92 ± 1.04	0.94 ± 1.04	0.93 ± 1.04	0.99 ± 0.97
	90	0.89 ± 0.95	0.91 ± 0.94	0.91 ± 0.93	0.99 ± 0.97

$$*\text{Ratio} = \frac{\text{Value}_{(Z_1,d_1)\% \text{ and } (Z_2,d_2)\%}}{\text{Value}_{10\% \text{ and } 60\%}}$$

Table 2 gave the absolute values for all contact point locations from different applied loads. However, Table 3 focuses on the relative results using a 0.5 nN applied force only with the chosen reference points ((Z_1, d_1) and (Z_2, d_2)) selected at 10% and 60% of the deflection. It is an overview of the absolute values of the contact point location results shown in Table 2 when selecting different reference points.

When choosing the reference point (Z_2, d_2) at a location lower than 50% of deflection, although the contact point did not fluctuate much, an increase not only in the fitting error (Eq. 11), but in the indentation length (calculated from the deflection and *z*-piezo displacement as described in Section 2.7) and number of fitted data points were also observed.

$$\text{Fitting error} = \sqrt{\frac{\sum\left(\mathrm{d}_{\mathrm{data}_i} - \mathrm{d}_{\mathrm{model}_i}\right)^2}{\mathrm{N}}} \qquad \text{Eq. 11;}$$

where N is the number of data points within a force curve, $\mathrm{d}_{\mathrm{data}_i}$ is the observed data point and $\mathrm{d}_{\mathrm{model}_i}$ is the modelled data point.

Additionally, in most calculations the standard deviations increased as well. The most dramatic increase in data variation was found when the (Z_2, d_2) reference was located below 25% of the maximum deflection curve. When selecting a (Z_2, d_2) above 50%, results did not display drastic changes. As standard deviations were lower for almost every factor, (Z_2, d_2) above 50% was identified as a workable reference to locate the contact point. However, reference (Z_2, d_2) should be carefully assessed for cases in which large applied loads are used, as the fittings may be influenced by substrate effects recorded by the deflection curves.

When compared to the results, locating the contact point by using a (Z_1, d_1) reference point at 15% instead of 10%, the standard deviation was similar. However, when using both 15%

and 25% as reference points, a smaller portion of the force curve was represented, generating a larger increase in the fitting analysis results and in the data variability.

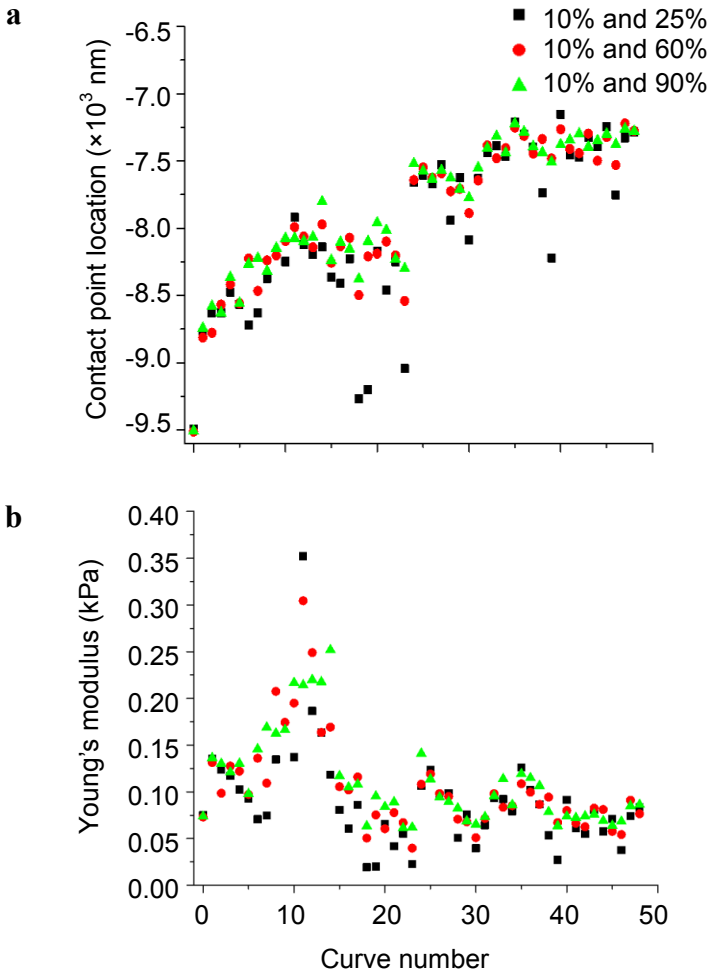

Figure 10. Contact point locations (a) and Young's modulus values (b) obtained by fitting the deflection-*z*-piezo displacement curves to the spherical model using different reference points (Z_1, d_1) and (Z_2, d_2) at 10% and 25% (black), 10% and 60% (red) and 10% and 90% (green) of the deflection. Total curves n=49 and 0.5 nN applied force were analyzed.

Figure 10 displays the contact point location (Z_0, d_0) and Young's modulus dependency of the reference points used to locate it. For each of the 49 deflection curves collected using a 0.5

nN applied force, the contact point was calculated by selecting three different pairs of (Z_1, d_1) and (Z_2, d_2) references at deflection positions of 10% and 25% (black), 10% and 60% (red) and 10% and 90% (green), to verify the consistency of the calculated contact point, respectively. 88% (43 curves out of 49) of the calculated contact point locations and Young's modulus values were different, while 12% (6 curves) were consistent. The three paired positions (Z_1, d_1) and (Z_2, d_2) as references to the contact point location (Eq. 10) showed the influence and importance of these reference points (Figure 10a). Young's modulus measurements using these same criteria are displayed in Figure 10b. Consistent contact point locations (*i.e.*, calculated contact points overlay), such as in curves #0, #5, #26, #32, #34 #36 and #49 (Figure 10a), resulted in consistency of the Young's modulus measurements (Figure 10b). When selecting 10% (d_1) and 25% (d_2), outliers such as in curves #18, #19, #23, #38 and #39 were observed (Figure 10a). This correlated to outliers of the measured Young's modulus values (Figure 10b).

Although contact point location was observed to increase throughout the 49 indentations of the NB4 cell (Figure 10a), this was likely due to the drift of the tip since the Young's modulus measurements were independent from that trend. When choosing the two reference points at deflections of 10% and 25%, only the beginning of the curves may comply with the models. Too many points on the curve were ignored, representing only a small indentation and superficial tip-sample contact. This information could not be easily seen in Tables 2 and 3 due to the large absolute value of the contact point locations between -9500 nm and -7000 nm within the *z*-piezo displacement range. Hence, only a small percentage difference was calculated in the contact point location (*e.g.* 100 nm changes only represent 1% variation in the contact point location).

Most of the data calculated using reference points at 10% and 60% (red), as well as at 10% and 90% (green) were more consistent with each other and did not display as deviated as

observed in the 10% and 25% data set (black), when using an applied force of 0.5 nN (similar fitting information can be found in Table 4 and Table 5 when using applied forces of 1.0 and 2.0 nN). When cells are indented using larger applied forces, substrate effects may become more obvious and (Z_2, d_2) should be positioned earlier on the deflection curve such as at 50% of the whole curve and not above 90%.

Table 4. Fitting analysis results for 49 force curves extracted consecutively using 1.0 nN applied force. Different reference points (Z_1, d_1) and (Z_2, d_2) were chosen. All results are compared to the reference at which (Z_1, d_1) and (Z_2, d_2) are set at 10% and 60%, respectively.

(Z_1, d_1) (% curve)	(Z_2, d_2) (% curve)	Average variation ratio of the fitting error* (± SD ratio)	Average variation ratio of the indentation length* (± SD ratio)	Average variation ratio of the number of data points* (± SD ratio)	Average variation ratio of the Z_0 location* (nm ± SD ratio)
	25	1.23 ± 1.26	1.19 ± 1.28	1.21 ± 1.43	1.03 ± 0.96
	50	1.05 ± 1.03	1.02 ± 0.99	1.02 ± 0.99	1.00 ± 0.98
10	**60**	**1.00 ± 1.00**	**1.00 ± 1.00**	**1.00 ± 1.00**	**1.00 ± 1.00**
	75	0.95 ± 1.01	0.96 ± 0.97	0.96 ± 0.92	0.99 ± 1.02
	90	0.95 ± 1.08	0.97 ± 1.05	0.96 ± 1.01	0.99 ± 1.05
	25	1.15 ± 1.20	1.11 ± 1.21	1.12 ± 1.30	1.02 ± 0.98
	50	0.98 ± 1.10	0.99 ± 1.09	0.99 ± 1.06	1.00 ± 1.04
15	60	0.90 ± 1.10	0.94 ± 1.07	0.94 ± 1.05	0.99 ± 1.05
	75	0.90 ± 1.14	0.92 ± 1.08	0.92 ± 1.05	0.99 ± 1.06
	90	0.42 ± 0.42	0.92 ± 1.14	0.91 ± 1.10	0.99 ± 1.09

Table 5. Fitting analysis results for 49 force curves extracted consecutively using 2.0 nN applied force. Different reference points (Z_1, d_1) and (Z_2, d_2) were chosen. All results are compared to the reference at which (Z_1, d_1) and (Z_2, d_2) are set at 10% and 60%, respectively.

(Z_1, d_1) (% curve)	(Z_2, d_2) (% curve)	Average variation ratio of the fitting error* (± SD ratio)	Average variation ratio of the indentation length* (± SD ratio)	Average variation ratio of the number of data points* (± SD ratio)	Average variation ratio of the Z_0 location* (nm ± SD ratio)
	25	1.08 ± 1.53	1.06 ± 1.67	1.06 ± 1.78	1.01 ± 1.10
	50	1.02 ± 1.03	1.01 ± 1.05	1.01 ± 1.06	1.00 ± 1.01
10	**60**	**1.00 ± 1.00**	**1.00 ± 1.00**	**1.00 ± 1.00**	**1.00 ± 1.00**
	75	0.98 ± 0.93	0.99 ± 0.98	0.99 ± 0.98	1.00 ± 1.01
	90	0.97 ± 0.82	0.98 ± 0.93	0.98 ± 0.93	1.00 ± 0.98
	25	1.05 ± 1.37	1.02 ± 1.27	1.02 ± 1.27	1.00 ± 1.08
	50	0.99 ± 1.13	0.99 ± 1.10	0.99 ± 1.08	1.00 ± 1.02
15	60	0.97 ± 1.06	0.99 ± 1.03	0.99 ± 1.00	1.00 ± 1.01
	75	0.96 ± 0.93	0.97 ± 0.98	0.97 ± 0.95	1.00 ± 0.99
	90	0.94 ± 0.85	0.97 ± 0.95	0.97 ± 0.93	0.99 ± 0.98

Finally, it is important to properly assess reference points used to locate the contact point as they not only influence the contact point location (Eq. 10), but also the fit Young's modulus values. Consistency in these reference points is crucial and should be standardized according to the specific AFM parameters used. In most of the NB4 cell indentation measurements, we choose to use 10% and 60% as the reference points to locate the contact point positions.

3.1.2 Comparison of the Fitting Models

As mentioned in Section 2.7, two fitting models were considered in the indentation measurements for calculating the Young's modulus. In this Section, multiple force indentation measurements were performed using different conical and spherical probes. Fitting values of Young's modulus were compared using the two modules.

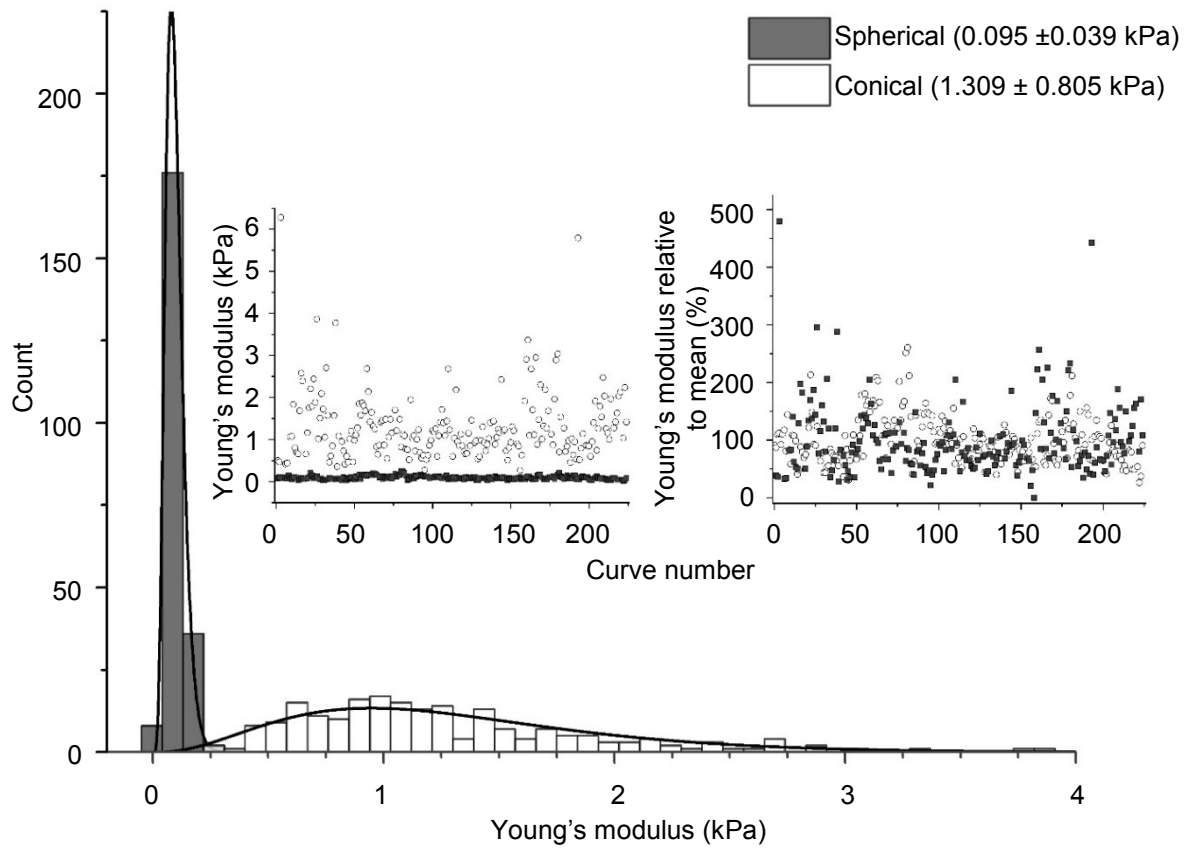

Figure 11. Representative Young's modulus values obtained from 250 deflection-displacement curves measured on individual NB4 cells under an applied load of 0.5 nN, using a conical and a spherical probe. Data were fit to the respective models (Eq. 8 and Eq. 9). Insets: Scattered plots of the Young's moduli for both probe types with respect to the curve number or relative to the average elasticity value for each curve.

Figure 11 displays the Young's modulus values using 250 force curves measured on NB4 cells. An applied force of 0.5 nN was used for both a conical probe and a spherical probe (20 μm in diameter) over different NB4 cells. Histograms represented the Young's modulus distributions when using either spherical or conical probes and fit to the respective models, namely Eq. 8 for the conical probe and Eq. 9 for the spherical probe. When using a conical probe and Eq. 8, a wider data distribution between 0.266 and 6.280 kPa were observed, when compared to the narrower distribution of 0.025 to 0.248 kPa when using a spherical probe (Eq. 9). For the 250

force curves, an average Young's modulus of 1.309 ± 0.805 kPa and 0.095 ± 0.039 kPa were calculated using a conical probe and a spherical probe, respectively.

The insets in Figure 11 show scattered plots of the Young's modulus values and variability obtained from 250 consecutive deflection-displacement curves for both probes. The left inset displays the same data set plotted in the histograms. It represented the data variability when using a conical or spherical probe. It was found that the data using the conical probe ended with a greater amount of outliers. However, when comparing the data variability with the average Young's modulus values (variability coefficient as shown in Eq. 12) for both the conical and spherical models, results were comparable (Figure 11, right inset). The relatively sharper probes (and fitting to the conical model, Eq. 8) may permit to detect local variations in elasticity on cell membranes instead of average elasticity with larger contact area when using a colloidal probe.

$$\text{Variability coefficient} = (100\% \cdot {}^{x_i}/_{\bar{x}}) \quad \text{Eq. 12;}$$

$$\text{Mean} = \bar{x} = \frac{1}{n}\sum_{i=0}^{n} x_i \quad \text{Eq. 13;}$$

In this context, it has been hypothesized that the data collected using a conical probe can be fit to the spherical model[74]. However, when fitting the data measured using a conical shaped probe to the spherical model with a probe radius of 50 nm, the same scattering was found in the plotted histograms, only the Young's modulus distribution was shifted to higher values. Fitting errors were higher when fitting the raw data with the inappropriate model. This indicates that when a conical probe is used to investigate the cells, a larger amount of data is required to properly represent the average elasticity of the cell membrane.

By varying the Young's modulus as a function of time, as demonstrated in the left inset of Figure 11, it is possible to determine the consistency of the collected data. The 250 consecutive curves measured by spherical probe showed a consistent Young's modulus, thereby indicating that using the 20 μm colloidal probes and fitting data to the spherical model provide uniform elasticity measurements. The conical model seemed, on the other hand, to provide a larger scattering of the data, suggesting less reliable elasticity measurements. However, by considering the variability coefficient of the data with respect to the mean measurement of the data set (Eq. 12 and Eq. 13), conical and spherical data are similar (Figure 11, right inset). As the absolute values of the Young's modulus are required for comparability and small mechanical property alterations are necessary to evaluate different types of cancer cells at different stages (or subjected to different treatments), the spherical model was deemed the best approach to investigate the APL-NB4 cells.

Insets in Figure 11 also helped identify cells that were influenced by their environment according to the magnitude of the differences in the elasticity values. This type of time-dependent Young's modulus measurements can also describe whether the cell has had enough time to relax between each tip-sample interaction by observing any time-dependent stiffening[5]. However, this is not the case in Figure 11, which included 250 force curves (13.33 min AFM collecting time, 0.5 nN applied force) using either model.

Lastly, the spherical probe was found to best represent average elasticity measurements of the NB4 cells, as it involves a larger tip-sample contact area and retrieves a narrower variability of the data. The conical probe also provides valid information of the cellular Young's modulus but its sharper shape may be associated to a greater penetration, which in turn may cause indentation of underlying organelles. For this reason, when using a conical probe, a larger

number of deflection curves are required to properly represent the average cell elasticity and observe any alteration of cell mechanics over time.

3.1.3 Assessment of Cell Tolerance to Externally Applied Forces

3.1.3.1 Comparison of Different Applied Forces

When performing the indentation measurements on cells, it is important to control and determine the proper applied forces and indentation lengths. In order to obtain statistically meaningful data, arrays of force-indentation measurements with different controlled forces were utilized to optimize the measurement conditions for NB4 cells.

Figure 12 shows the assessment of the elasticity when indenting different NB4 cells with the conical and the spherical probes using different applied loads. Any data points further than 1.5 times of the inter-quartile range (IQR) are labeled as outliers. Each box plot represents collected data from a single cell probed 49 times. Five different cells were considered to evaluate each applied load. For the assessment of each probe, 3 different conditions were considered, namely applied loads/forces of 0.5, 1.0, and 2.0 nN. All fittings were performed by fixing (Z_1, d_1) and (Z_2, d_2) at 10% and 60% of the deflection with respect to the whole curve, in order to locate the contact points (Table 6).

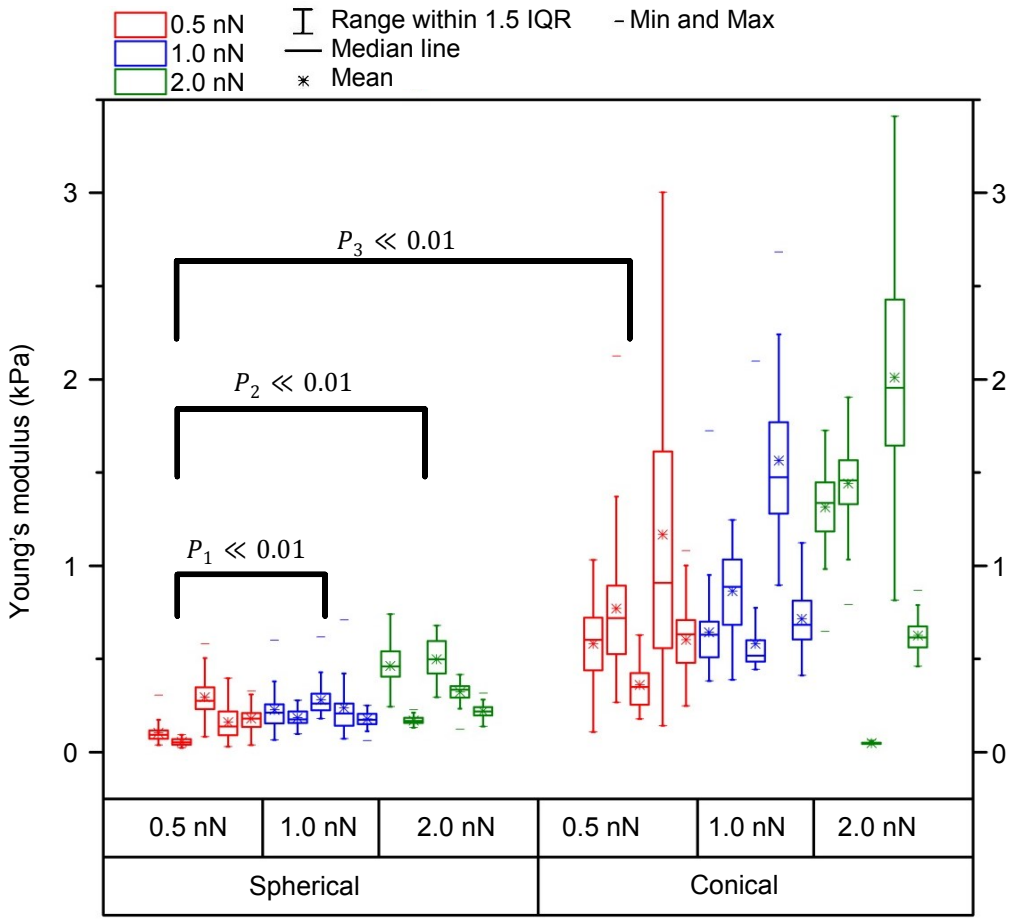

Figure 12. Elasticity measurements on 5 different NB4 cells for each assessed applied forces of 0.5, 1.0 and 2.0 nN, respectively, using both a spherical probe and a conical probe. Young's modulus values were obtained by fitting 49 deflection-displacement curves to the respective models. Average (mean) Young's modulus values for single NB4 cells are labeled by square points within each box plots. Labeled *P* values, calculated from two-sample t-test are displayed.

When considering the applied forces for cells probed with the spherical indenter, elasticity values increased upon raising the applied force to 2.0 nN. In particular, upon increasing the applied load from 0.5 to 1.0 and 2.0 nN, a mean Young's modulus of 0.16 ± 0.07 kPa was obtained for an applied load of 0.5 nN, which increased to 0.22 ± 0.08 kPa and 0.34 ± 0.06 kPa at 1.0 and 2.0 nN, respectively. The same trend was observed with a conical probe when using the same load increments. However, unlike the previous case, changes were also observed

between 0.5 and 1.0 nN. In fact, with a 0.5 nN force, the average elasticity was 0.70 ± 0.34 kPa, 0.87 ± 0.25 kPa for 1.0 nN, and 1.09 ± 0.22 kPa for 2.0 nN (conical probe, Eq. 8, in Table 6). Therefore, in agreement with results shown in Figures 11 and 12, measurements using a conical probe (fitting to conical model) might be associated to larger and more scattered Young's modulus values than those obtained with the spherical model (using 20 μm spherical probes). Such large variability in Young's modulus measurements may be explained by considering the probe's larger sensitivity to underlying organelles due to the concentrated stress exerted by conical tips. In fact, smaller applied forces are required to indent smaller depth of the cell membrane when using a sharper probe. Cells thus appear to better tolerate the indentation of a large sized spherical probe, rather than that of a sharper conical probe.

A two-sample t-test revealed that the mean Young's modulus values are significantly different ($P \ll 0.01$) when using these different applied forces with either conical or spherical probes. In Figure 12, all data between groups (spherical and conical models) or subgroups (0.5, 1.0 and 2.0 nN applied forces) were significantly different. In addition, as expected, when comparing the 0.5 nN applied force to the 1.0 nN applied force within the spherical probe group, the probability of having similar groups was larger than when comparing the 0.5 nN subgroup to the 2.0 nN subgroup. Moreover, due to the variability in the conical probe data, 0.5 nN applied force between the spherical and the conical groups, the calculated probability was slightly lower than when comparing the 0.5 nN force and 2.0 nN within the spherical groups ($P_3 < P_1 < P_2 \ll 0.01$).

Table 6. Elasticity measurements on 5 different NB4 cells for each assessed force applied of 0.5, 1.0 and 2.0 nN, respectively, using both a spherical probe and a conical one. Young's modulus values were obtained by fitting 49 deflection-displacement curves to the respective models.

Force (nN)	Model	Cell (% curve)	Minimum Young's Modulus (kPa)	Maximum Young's Modulus (kPa)	Average Young's Modulus (kPa ± SD)	Overall average of the Young's Modulus (kPa ± SD)
0.5	Spherical	1	0.038	0.304	0.104 ± 0.052	**0.159 ± 0.066**
		2	0.023	0.094	0.055 ± 0.017	
		3	0.082	0.581	0.295 ± 0.097	
		4	0.030	0.398	0.161 ± 0.099	
		5	0.038	0.328	0.180 ± 0.067	
	Conical	A	0.109	1.031	0.582 ± 0.202	**0.697 ± 0.339**
		B	0.267	2.123	0.771 ± 0.386	
		C	0.178	0.627	0.361 ± 0.125	
		D	0.142	3.002	1.166 ± 0.796	
		E	0.247	1.079	0.603 ± 0.186	
1.0	Spherical	6	0.065	0.601	0.228 ± 0.100	**0.222 ± 0.082**
		7	0.097	0.278	0.185 ± 0.043	
		8	0.181	0.617	0.281 ± 0.090	
		9	0.072	0.709	0.237 ± 0.137	
		10	0.062	0.251	0.178 ± 0.039	
	Conical	F	0.383	1.723	0.643 ± 0.208	**0.874 ± 0.249**
		G	0.388	1.245	0.863 ± 0.231	
		H	0.443	2.096	0.582 ± 0.244	
		I	0.895	2.682	1.563 ± 0.396	
		J	0.411	1.123	0.716 ± 0.167	
2.0	Spherical	11	0.244	0.740	0.462 ± 0.105	**0.335 ± 0.063**
		12	0.131	0.226	0.170 ± 0.020	
		13	0.294	0.679	0.498 ± 0.107	
		14	0.123	0.415	0.323 ± 0.049	
		15	0.138	0.316	0.222 ± 0.036	
	Conical	K	0.647	1.725	1.314 ± 0.211	**1.088 ± 0.222**
		L	0.792	1.903	1.441 ± 0.226	
		M	0.042	0.064	0.049 ± 0.005	
		N	0.815	3.410	2.009 ± 0.570	
		O	0.459	0.867	0.626 ± 0.095	

3.1.3.2 Comparison of Different Cell Indentation Lengths

The indentation length of the force curve measured on NB4 cell was fully assessed, in order to find the optimized indentation length that should be used to analyze this specific cancer cell type. A 7 by 7 force map grid was set to measure over single NB4 cells. In order to avoid any substrate effect due to different sizes of cells, a maximum load of 0.5 nN was used in this study. Using such a small force may also help avoid any influence of underlying organelles to ensure that only the cell membrane is being probed.

Table 7. Young's modulus dependency of the fitted indentation length of 49 force curves extracted consecutively over a single NB4 cell using an applied load of 0.5 nN and spherical probe and model.

Defined indentation length (nm)	Measured Indentation length (nm)	Minimum indentation length (nm)	Maximum indentation length (nm)	Average Young's Modulus (kPa ± SD)	Minimum Young's Modulus (kPa)	Maximum Young's Modulus (kPa)
200	199.94 ± 0.32	198.89	200.61	0.164 ± 0.106	0.077	0.677
400	399.83 ± 0.27	399.29	400.55	0.110 ± 0.059	0.029	0.325
600	596.36 ± 16.88	488.19	600.64	0.103 ± 0.054	0.020	0.304
800	766.04 ± 76.49	488.19	800.74	0.103 ± 0.053	0.023	0.304
1000	892.80 ± 148.71	488.19	1000.45	0.103 ± 0.053	0.030	0.304
Whole curve	998.54 ± 257.76	488.19	1612.69	0.104 ± 0.052	0.040	0.304

Figure 13 displays the representative Young's modulus dependency of the fit indentation length. 49 force curves were consecutively collected using a 0.5 nN applied load over a single NB4 cell by 20 μm spherical probes. Curve fittings were performed to fit the deflection-displacement data to the spherical model. All 49 curves were fit by restricting the indentation length to different values, all starting from the calculated contact point located using reference points at 10% (Z_1, d_1) and 60% (Z_2, d_2). Six different Young's modulus values were calculated for each force curve using fit apparent indentation lengths of 200 nm, 400 nm, 600 nm, 800 nm, 1000 nm and the full indentation length. Data is displayed in Table 7.

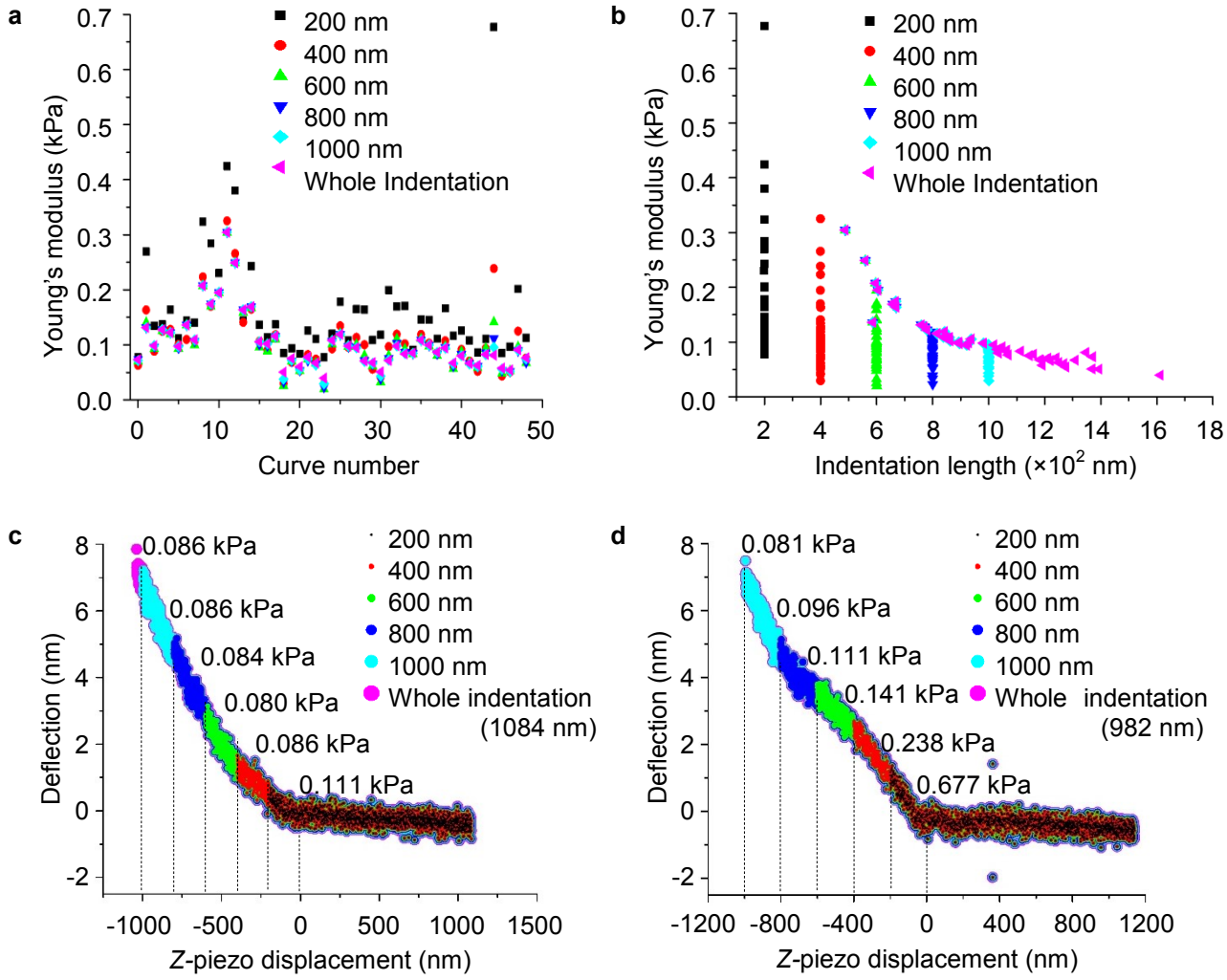

Figure 13. Young's modulus dependency of the fit indentation length of 49 force curves measured consecutively over a single NB4 cell using an applied load of 0.5 nN and spherical probe and model. Young's modulus values plotted as a function of curve number (a), indentation length (b), and fit to different indentation lengths with two representative force curves (number 37 (c), and number 44 (d)).

When different indentation lengths were selected to fit the same force curve, the Young's modulus varied accordingly. Figure 13a presents the Young's modulus as a function of the curve number using different indentation length. On the other hand, Figure 13b displays the Young's modulus as a function of indentation length alone, also showing the change and spreading levels in data variability when fitting the same curves (as in Figure 13a) using different indentation

lengths. When fitting the curves by setting the apparent indentation to 200 nm and 600 nm, the mean Young's modulus values were 0.164 ± 0.106 kPa, and 0.103 ± 0.054 kPa, respectively. As shown in Figure 13b, spreading of the data was also found larger using a 200 nm indentation length. When performing two-sample t-tests with respect to the full indentation length of the deflection curves, only the apparent indentation length of 200 nm was revealed to significantly differ from the fittings performed using the full deflection curve ($P \ll 0.01$).

Figures 13c and 13d represent individual deflection-z-piezo displacement curves that were fit using the different indentation lengths. Curve #37 (Figure 13c) demonstrates the ideal smooth curve which obeyed the fitting model quite well. When increasing the apparent indentation length from 200 to 1000 nm, Young's modulus values varied from 0.11 to 0.08 kPa. However, in the case of a non-ideal curve, such as in Figure 13d, fittings using similar apparent indentation lengths (200 to 1000 nm) resulted in a decrease of the Young's modulus from 0.68 kPa to 0.09 kPa. This clearly shows the importance of preselecting the proper indentation parameters during data collection to avoid inconsistency of the fitting results.

It should be noted that in both Figures 13a and 13b, when the full indentation length of the curve ranged below the selected apparent indentation length, the full indentation length was used to fit the curve. For example, a curve with an indentation length of 500 nm would be fit to 500 nm for a selected 600, 800 or 1000 nm as apparent indentation. This occurrence was observed in Figure 13b when the Young's modulus values were repeated for indentation length other than those selected (*i.e.,* other than 200, 400, 600, 800, 1000 nm). In other words, when the maximum indentation length was set to a value smaller than that of the whole curve, the entire force curve was fit, causing *false* overlays of the fitted data (Figures 13a and 13b). For example, curve #12 involves identical Young's modulus measurements of 0.249 kPa when using

indentation length of 600 nm and higher as the indentation length of the whole curve was 559.92 nm (Figures 13a and 13b).

Finally, a minimum indentation length of 600 nm should be considered to avoid scattering of the data and avoid the influence of shallow contact or keep contact area as consistent as possible during data collection. It is important to understand that when substrate effects need to be avoided, limiting the indentation length during fittings to correct the use of a large applied force is not a solution. When using a small force such as 0.5 nN, the whole curve should be fit in order to maintain consistent and comparable fittings. This avoids biased elasticity measurements and is an important factor to consider when collecting force curves. AFM parameters should not be altered for fitting purposes after data collecting, in order to maintain consistency within the applied force used. Maximum applied load and scan length should be optimized prior to data analysis, to avoid misleading results.

3.2 Probing ATO Treated NB4 Cell Elasticities

From the optimized analysis process outlined in Section Chapter 3, viability, elasticity and morphology of ATO treated NB4 cells were assessed. Viability assays were first performed in order to determine a workable ATO drug concentration which provides insightful information on the drug effects in a reasonable timeframe within which experiments can be carried out. Morphology and cell elasticity were then assessed in order to evaluate the effects of ATO.

3.2.1 Viability Tests

3.2.1.1 Trypan Blue Staining

This Thesis' main objective was to monitor the effects of ATO on NB4 cells with the dosage concentration as close as possible to standard therapeutical protocols in terms of drug dosage. The first series of experiments was performed by using Trypan Blue staining, which allowed identifying the proper ATO concentration in order to complete experiments in a reasonable post-treatment timeframe.

Cell culture flasks containing approximately 4×10^4 cells/mL were treated with a single dose of ATO at different concentrations. Two sets of drug treatments with 3, 10 and 30 μM (Table 8), and with 10, 20 and 30 μM (Table 9) were evaluated independently. Cell viability from 6 different samples for each treatment (flask) was monitored overtime for both the negative (blank cell solution) and positive (PBS treated cell solution) controls, along with the three additional ATO treatments.

Table 8 displays the viability test results obtained by quantifying Trypan Blue stained cells over a hemocytometer. The PBS treated cells (PBS in Table 8) behaved similarly to the blank cells over a testing period of 96 h, indicating that the PBS did not significantly affect the cell viability. Within 96 h, neither control revealed any significant viability changes although cell counts kept increasing from 4.2×10^4 cells/mL (0 h) to 10^5 cells/mL (96 h), as cells are expected to differentiate.

Table 8. Viability results of blank, PBS and 3, 10 and 30 µM ATO treated cell solutions over 96 h (sampling number n=6).

	Time after treatment (h)				
	0-2	**24-26**	**48-50**	**72-74**	**96-98**
	Average viability ± standard deviation (%)				
Blank	99.5 ± 0.8	98.6 ± 1.0	99.1 ± 0.6	98.9 ± 0.9	98.6 ± 0.4
PBS	97.8 ± 1.3	98.2 ± 1.1	98.9 ± 0.7	98.0 ± 0.3	98.6 ± 0.6
3 µM ATO	98.7 ± 0.8	95.5 ± 1.3	65.4 ± 9.6	15.1 ± 4.1	1.4 ± 1.4
10 µM ATO	99.2 ± 1.1	78.5 ± 6.5	6.7 ± 4.7	1.3 ± 1.6	1.0 ± 1.4
30 µM ATO	97.4 ± 1.8	50.6 ± 4.2	0.0 ± 0.0	0.0 ± 0.0	0.0 ± 0.0

When treating cells with 3 µM ATO, viability decreases significantly as soon as 48 h post-treatment. Between 48 and 72 h, viability decreases by 50%, which represents the largest monitored decrease in viability. Up to 96 h after ATO treatment, only few viable cells could be counted.

Furthermore, when studying concentrations over 10 µM ATO, cell viability beyond 48 h after treatment did not display important effects, since the majority of treated cells were observed to have already broken (stained). These higher drug concentrations were thereby identified as good candidates to carry out experiments within a reasonable timeframe.

The 30 µM ATO treatment displayed the particularity of 3 major viability measurements from 0 to 48 h post-treatment. Cell viability decreased of 50% within the first 24 h and samples did not seem to involve any viable cell at 48 h post-treatment. These rapid alterations in viability will require further analysis to determine the consistency of the data and cell behavior.

Table 9 displays repeated viability tests performed by focusing on the higher drug concentrations tested, *i.e.* 10, 20 and 30 μM. Drug treatments were monitored for a shorter time period of 48 h during which more drastic drug effects could be seen, compared to the results in Table 8. After 24 h, a decrease in cell viability could be observed in all ATO treated samples. For the 10, 20 and 30 μM ATO treatments, cell viability decreased from nearly 100% to 81.7 ± 9.4%, 84.2 ± 6.0% and 35.8 ± 7.2% respectively within 24 h. Theses quick assessment exposed the potential in using a 30 μM treatment in order to monitor noticeable viability changes in a short time. This provides an opportunity in investigating time sensitive drug effects.

Table 9. Viability results of blank, PBS and 10, 20 and 30 μM ATO treated cell solutions over 48 h (sampling number n=6).

	Time after treatment (h)		
	0-2	**24-26**	**48-50**
	Average viability ± standard deviation (%)		
Blank	98.4 ± 0.6	99.5 ± 0.4	99.5 ± 0.4
PBS	100.0 ± 0.0	98.7 ± 1.4	98.0 ± 0.6
10 μM ATO	99.7 ± 0.7	81.7 ± 9.4	8.0 ± 5.6
20 μM ATO	99.2 ± 0.6	84.2 ± 6.0	1.3 ± 0.5
30 μM ATO	97.9 ± 0.9	35.8 ± 7.2	0.0 ± 0.0

3.2.1.2 Microplate Fluorescence Intensity Readings

In order to gather larger amount of viability data, microplate fluorescence intensity readings were performed. Although population dependent, these assays facilitate maintaining consistent experimental conditions specifically as measurement timing are more accurate and collect a larger amount of data.

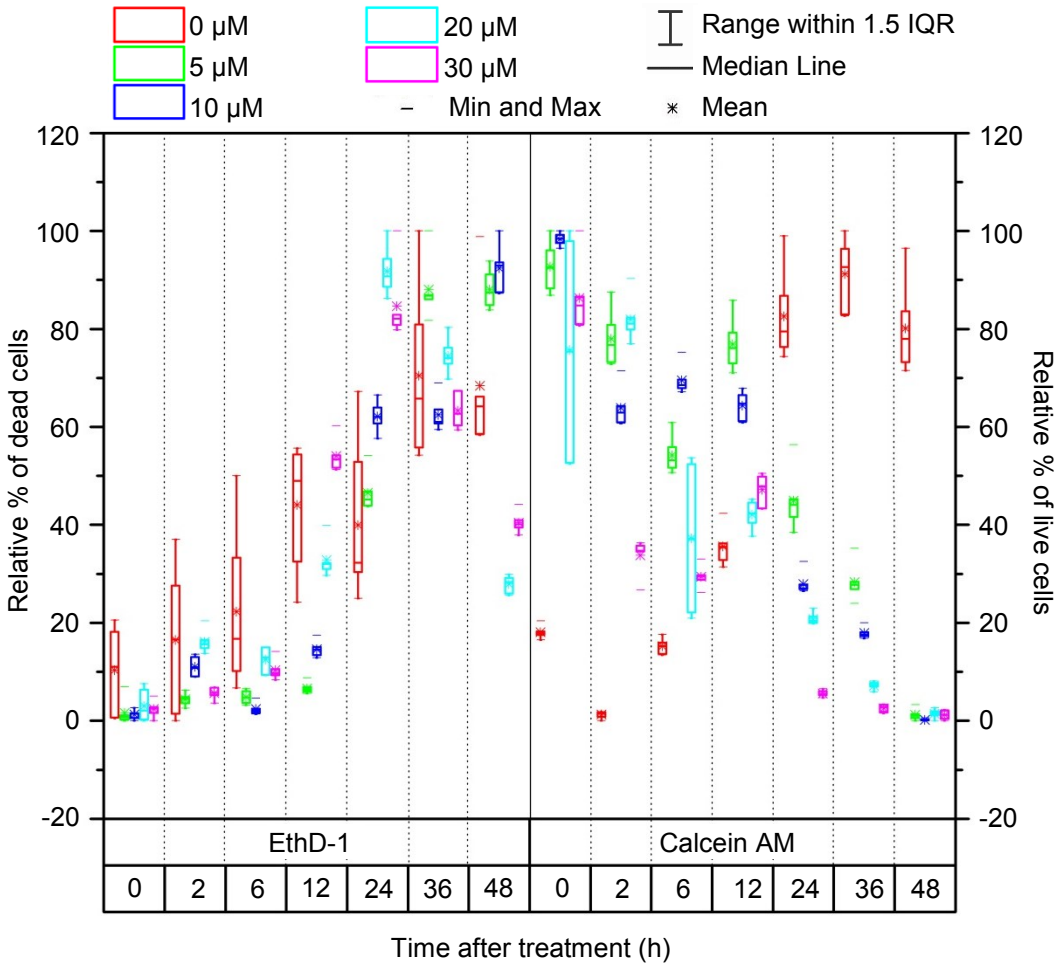

Figure 14. Microplate fluorescence intensity readings using a LIVE/DEAD viability kit with ethidium (EthD-1) and calcein AM to label dead and live cells, respectively. Measurements were taken for cells treated with 0, 5, 10, 20 and 30 μM ATO, from 0 to 48 h after treatments. Each box plot represents 48 measurements from 48 independent microplate wells.

Figure 14 represents microplate fluorescence intensity readings performed to compare the relative population of both live and dead cells overtime using different ATO concentrations. A LIVE/DEAD viability/cytotoxicity kit using ethidium (EthD-1) to measure the relative amount of dead cells and calcein AM to measure the relative amount of live cells was used. The relative dead or live cell ratios upon treatments of ATO at different time after treatment (0, 2, 6, 12 and up to 48 h after ATO treatments) are displayed in Figure 14. Each point in the box plot

represents 48 fluorescence intensity measurements within the 96-well plate. The second half of the microplate wells were used for control purposes to measure effects of the PBS and DMEM cell media, in order to subtract background from the intensity readings. These assay tests allowed a large amount of measurements obtained within a short period of time.

Overall, the fluorescence intensity readings indicated an increase in dead cell populations within 48 h after drug treatment. For the 0 μM treated cells, larger standard deviations were calculated between 9 and 17% compared to the other treatments involving ATO. Using either a 5 or 10 μM ATO concentrations, the largest amount of the dead cells is found at 36 h post-treatment. Larger treatment concentrations of 20 or 30 μM were found to have a larger amount of dead cells as early as 12 h, and mostly at 24 h post-treatment. With respect to live cell populations, the largest standard deviations are measured at 0 and 6 h post-treatment using 20 μM ATO, measured at 24% and 15%, respectively. Due to cell division, the 0 μM treated cells involved an increase in live cell populations. Other treatments were shown to have a decrease in viable cell until 48 h post-treatment, at which point, standard deviations were shown $< 1\%$.

When taking a closer look at the effects of the 30 μM ATO treatments, the data distribution appeared much narrower when compared to the other ATO treatments. This outcome indicates that the ATO drug has significant effects on most of the NB4 cells when using 30 μM ATO. At earlier and later stages, the dead and live cell populations are also observed to be accurately measured, creating reliable reference points for AFM experiments (Section 3.2.3).

Another particularity when using 30 μM is the presence of a timeframe within which drastic increase in dead cells and decrease in live ones can be observed. Those changes are

shown in Figure 14 between 6 and 24 h after treatment. Within that time window, the cells were highly affected by the treatment and underwent significant viability changes.

In terms of apoptosis stages, an increase in cell death is characteristic of the drug effects. EthD-1 was observed to bind with DNA within only 2 h. A drastic increase in DNA breakage occurred between 6 and 24 h post-treatment, which is in agreement with karyorrhexis (nucleus fragmentation). Furthermore, decreases in both live and dead cell populations (both fluorescence intensities) are an indication that although the live cells are transferred to the dead cell population, which is likely due to a larger amount of dead cells degrading and thus the decreased fluorescence intensity (between 24 and 36 h post-treatment, dead cell degradation likely occurs more frequently than the death of live cells). Finally, as expected at 48 h, live cell populations decreased to almost zero and cell division was interrupted throughout the treatment.

In summary, viability assays suggest some possible predictions on cell morphology changes, which may agree with the theoretical apoptosis stages discussed in the Introduction. Now, concrete morphology evaluation is necessary, in order to observe the evolution of the drug-programmed cell death. These fluorescence assay measurements also permitted to identify a proper drug concentration of 30 μM, which was found to induce quick alterations in cell physical alternation and possibly mechanical changes. These will be assessed in Sections 3.2.2 and 3.2.3.

3.2.2 Morphology Assessment

As mentioned in the Introduction and Section 3.2.1.2, apoptosis stages are usually closely related to the cell shape and size changes. Here, drug induced cell morphology alternation will be determined using optical microscopy and SU8-10 microwells.

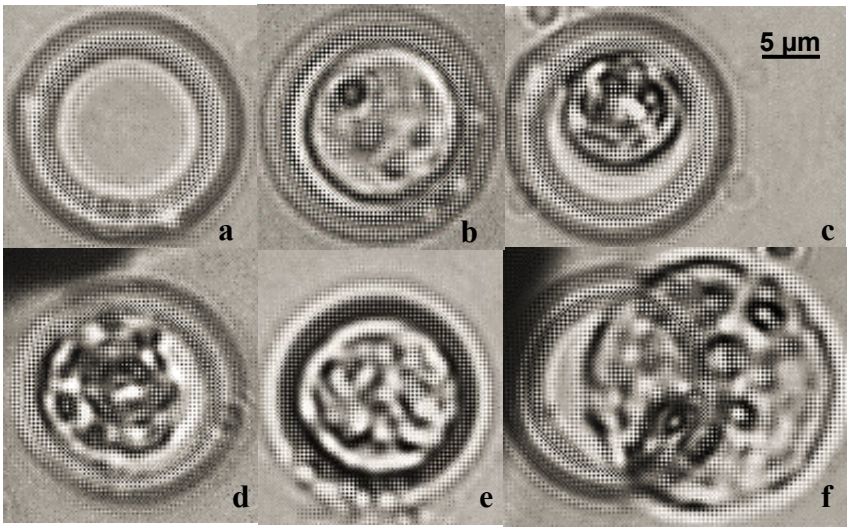

Figure 15. Images of an empty SU8-10 well (a), a round NB4 cell within an SU8-10 well at 0 h after treatment (b), a shrunk NB4 cell 12 h after treatment (c), advanced cell blebbing observed at 24 h after treatment (d), a cell with an unclear boundary 36 h after treatment (e) and cell swelling observed 12 h after treatment (f). Treatments were performed using 30 µM ATO.

Images of representative cell morphology can be observed in Figure 15. An empty well is displayed in Figure 15a, to facilitate the identification of cells within the wells, as well as the scaling of the cell size. Figure 15b represents most of the round cells found at 0 h post-treatment. Due to their geometry, these were ideal for measuring cell diameters. Figure 15c characterizes cells that have undergone cell shrinkage and possibly pyknosis, mostly found at 6 and 12 h post treatments. These cells displayed obvious decrease in size while maintaining their circular shapes. At 24 h post-treatment, cells showed advanced signs of blebbing as they appeared to possess irregular membranes and did not have a specific measurable diameter (Figure 15d). Blebbing could also be observed in 20% of the cells at 12 h post-treatment. At 36 h post-treatment, cell membranes are barely identifiable as the microwells contain multiple cell fragments, see Figure 15e.

Necrotic cell death could also be observed. However, as displayed in Figure 15f, necrosis causes cells to swell, restricting their access to the microwells. The microwell array substrate revealed itself as a good tool in sorting both cell death processes in addition to trapping the NB4 cells.

Table 10. Average cell diameters (µm) of 10 cells measured at each monitored time after ATO treatments (h).

Time after treatment (h)	Cell diameter Average ± Standard Deviation (µm)	Increase (+) and decrease (-) in diameter (%)
0	12.3 ± 1.2	---
2	12.4 ± 1.5	+0.8
6	11.2 ± 1.2	-8.9
12	10.4 ± 1.8	-15.5
24	~10.9 ± 2.1*	-11.2
36	~11.2 ± 1.4*	-8.9
48	~10.3 ± 1.6*	-16.3

*Approximate diameter measurements as cells no longer appeared round.

Table 10 reports the average cell diameter measured for each monitored time after 30 µM ATO treatments, as well as the percentage of cell diameter changes compared to the average cell diameter measured at 0 h post-treatment. From 0 to 12 h post-treatment, obvious cell shrinkage and condensation could be observed. However, between 24 and 48 h cell diameter measurements became an imposition as they did not possess their initial round shape. Irregular membranes and fragments were observed in that time period.

As cell morphology evolution can effectively help in identifying apoptosis stages, it does not reveal when internal changes occur; whereas AFM would provide sensitive mechanical

responses. Thus correlations among viability, morphology and elasticity upon indentation may provide insights in understanding specific physical and biological effects on the APL cancer cells.

3.2.3 Elasticity and Indentation Measurements

AFM indentation measurements were performed to monitor the drug effects on cell mechanics. Figure 16 displays the Young's modulus (a) and maximum indentation length (nm) before reaching a maximum applied force of 0.5 nN (b) for different cells at different times after being treated using a 30 μM ATO concentration. Each box plot represents 49 indentations over a single cell.

Table 11 presents the average mean Young's modulus and average mean standard deviation for all 10 cells at each time spot. For control purposes, the SU8-10 substrate was also indented using the same AFM conditions as for the NB4 cells. Young's modulus over a flat surface of the substrate is of 509 ± 389 kPa. These allowed determining whether data was extracted over the substrate instead of the cell surface as linear force curves could be observed due to the harder material.

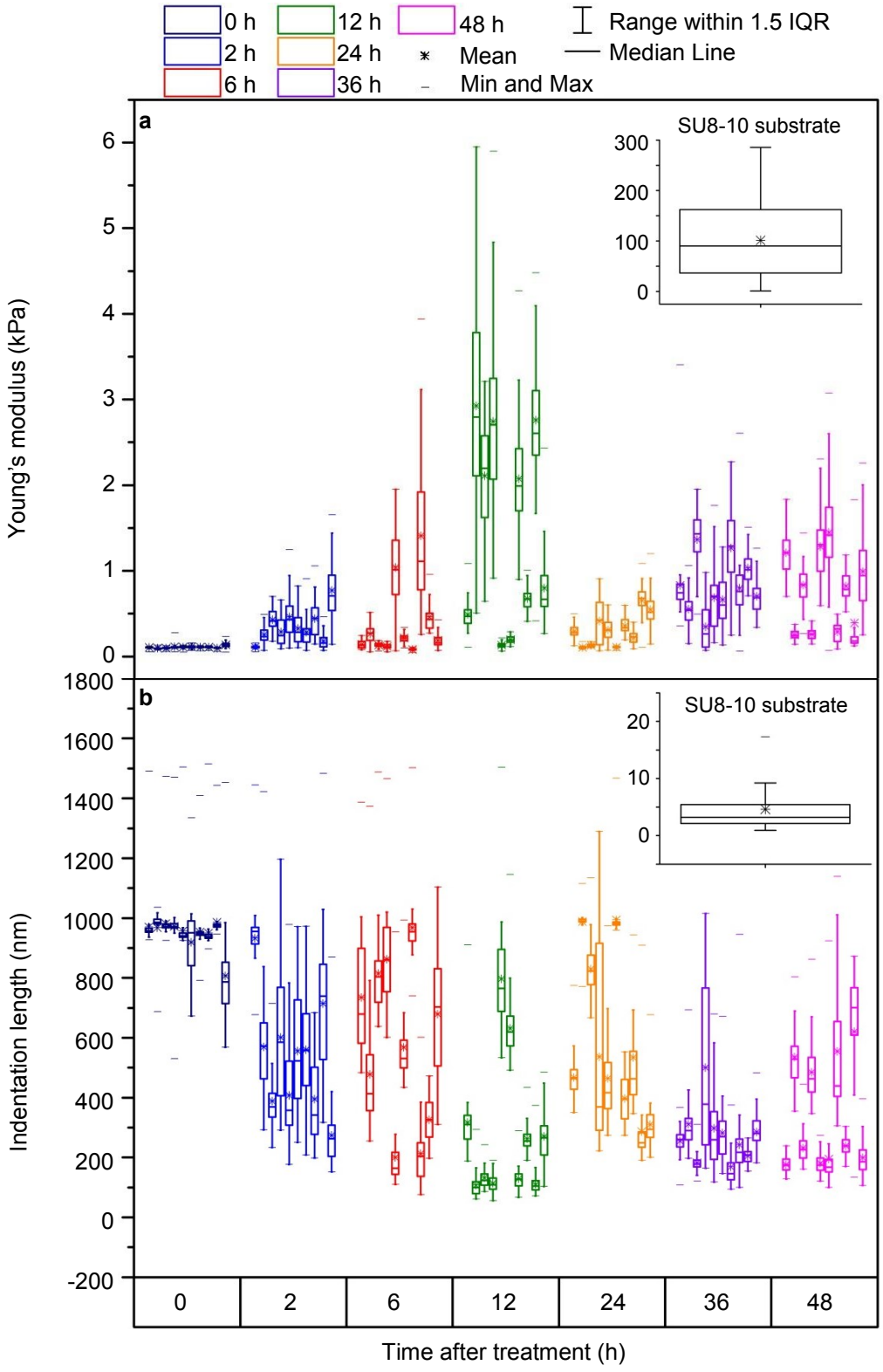

Figure 16. Young's modulus (a) and maximum indentation length (b) distributions of NB4 cells at different times from 0 to 48 h after 30 µM ATO treatments. For each monitored time after treatment, 10 different cells were measured. Each box plot represents each of those cells that were indented 49 times. Insets: Young's modulus (a) and maximum indentation values (b) of the substrate were generated from AFM indentations over the SU8-10 flat surface and microwell for control purposes.

Table 11. Average Young's modulus (Pa) and indentation length (nm) of NB4 cells at each monitored time after 30 μM ATO treatments. Each result represents the average of the 10 measured cells. 49 indentations over the SU8-10 surface were recorded for control purposes.

		Young's modulus Avg ± SD (Pa)	Indentation length Avg ± SD (nm)
Time after treatment (h)	0	108 ± 19	946 ± 102
	2	355 ± 250	540 ± 245
	6	455 ± 557	565 ± 292
	12	1488 ± 1233	288 ± 242
	24	315 ± 220	579 ± 289
	36	827 ± 437	271 ± 151
	48	780 ± 541	341 ± 211
SU8-10 substrate	Flat surface	$509 \times 10^3 \pm 389 \times 10^3$	5 ± 4

At 0 h treatment, a narrower distribution of the Young's modulus values was observed. However, as soon as 2 h after 30 μM ATO treatment the elasticity distribution was observed to widen, which may be explained by the fact that different cells may respond differently to the treatment. At 2 and 6 h after treatments, elasticity results increased from 355 ± 250 Pa to 455 ± 557 Pa respectively. Cells were found the stiffest at 12 h after treatment with 1488 ± 1233 Pa, where the data distribution was also the widest. This is not in agreement with the viability assay measurements (Figure 14, Section 3.2.1.2), as the largest amount of red emitting fluorescence found at 24 h post-treatment, while Young's modulus results shown the largest at 12 h post-

treatment. We can therefore conclude that 24 h post-treatment likely represented the point at which cell membranes ruptured. At later treatment stages, 24, 36 and 48 h post-treatments, Young's modulus decreased and did not display any drastic changes and no data pattern could be identified (Figure 16).

Two-sample t-tests were performed to compare Young's modulus results at each monitored time after treatments. P values revealed that the Young's moduli involved significantly different mean values ($P \ll 0.01$), except for Young's modulus measurements at 36 and 48 h, which were shown not to be significantly different (P=0.237). This most likely represents the time at which cells have already broken into apoptotic bodies.

Similarly observed in the fluorescence viability assays measurements, the most important changes in the elasticity measurements occur between 6 and 24 h after ATO treatments. These results may indicate that the previous analysis of apoptosis stages in viability assays may also be tracked through cell mechanics. During cell shrinkage, the cytoskeleton is broken down, and can no longer help in cell motility and structure. It densifies and as there is less spacing between the cellular components, it may contribute to an increase in Young's modulus. Another factor that would increase cell elasticity occurs early within the chromatin condensation phase (pyknosis). In this study as drug effects do not uniformly affect cells as they experience apoptosis at different times after treatment, cell shrinkage and pyknosis may be observed throughout the first 12 h post-treatment. Once the fragmentation of the nucleus (karyorrhexis) follows, this may be found to soften the cell for a short period of time as a little more space might be found for intracellular components. These may explain a few data points with the decrease of Young's modulus between 2 and 6 h post treatments. In any case, once the cell membrane is broken and cell fragments are dispersed into apoptotic bodies, a large decrease in cell elasticity should be

observed, as the cell internal pressure is released. This is consistent with the data shown in Figure 16, between 12 and 24 h post-treatments when using 30 μM ATO. Once the cell is fragmented, no pattern in elasticity could be found as different shapes and apoptotic body aggregations could be measured within the SU8-10 microwells. These may also include more significant substrate effects.

A similar analysis was performed by comparing maximum indentation lengths to reach a maximum applied force of 0.5 nN using the same cell data as for the elasticity measurements. As a result, harder cells can be identified as they involve lower indentation lengths. However, these indentation measurements may provide additional information on the consistency of the indented sample. Similar maximum indentation length controls were evaluated over the SU8-10 substrate as measured for the Young's modulus. In the inset of Figure 16a, the maximum indentation length measured over a flat surface of the substrate is of 5 ± 4 nm.

As shown in Section 3.1.3, NB4 cells without ATO treatment did not show mechanical alterations when indented 49 times using the spherical probe with the 0.5 nN maximum applied force. Indentation lengths were also a good indication and reflection of cell elasticity. As the elasticity of the cells increase, the maximum indentation length decreases. Again, once treated, NB4 cells became harder up to 12 h post-treatment.

Figure 16b displays the maximum indentation length of 10 different cells indented 49 times each. The same data set to extract Young's modulus measurements (Figure 16a) was used for comparison purposes. As expected, the maximum indentation lengths decreased up to 12 h after treatments using a 30 μM ATO concentration. Hardening and softening of the cells concur in both the Young's modulus and maximum indentation length. The data variation however

behaved differently than that of the Young's modulus. This may be explained as the real-time measurements do not represent the *ideal* indentation curves.

Average of the maximum indentation lengths decreased from 0 to 12 h by 70%, although no changes could be observed between 2 and 6 h post-treatments (see Table 11). At 24 h after treatment, maximum indentation length reached a mean average of 579 ± 289 nm. However at 36 and 48 h after treatments, indentation lengths decreased up to 271 ± 151 nm and 341 ± 211 nm, respectively, indicating that cell indentations may involve larger substrate effects at this point. This may be explained by the measurements were performed on the small apoptotic bodies, not the intact cells.

CHAPTER 4: CONCLUSION

4.1 Summary

The Thesis work was first set out to explore the alterations in viability, morphology and elasticity of NB4 cancer cells derived from acute promyelocytic leukemia upon arsenic trioxide (ATO) drug treatments. However, cell elasticity measurements through AFM required optimized sample-specific data collection and analysis procedures. In order to complement the existing literature, we have developed an automated batch analysis code to perform un-biased data processes on AFM indentation data measured over leukemia cancer cells. Both AFM experimental parameters such as probe selection, maximum applied force and, as well as fitting criteria including contact point location and indentation lengths were optimized and reported in this Thesis.

By confining the non-adherent NB4 cells into SU8-10 microwell arrays, it was possible to systematically study the mechanical properties of these cells by AFM based force indentation measurements. A significant amount of raw data was collected, in order to provide reference elasticity values for untreated NB4 cells. Applied forces and indentation lengths, the measurement velocity and substrate treatments were found to be important parameters before and during the data compiling. Additional criteria, such as the location of the contact point and the selection of adequate contact mechanics models, were essential to properly fit the indentation portion of the force curves. Thus, several fitting criteria were defined to best optimize data processing and obtain consistent and comparable results. The contact point location was reliably found by using the two-reference-point approach, (Z_1, d_1) and (Z_2, d_2), at 10% and 60% of the deflection, respectively. Although both conical and spherical models were studied, the spherical probe was found to be more appropriate for the APL cancer cell detection by better representing

the average Young's modulus, with narrow distributions. Furthermore, a range of applied forces and cell indentation lengths were assessed, in order to improve force curve collections over NB4 cells by identifying applied load magnitudes that reduce cell damage, substrate effects, as well as shallow indentation. Results in Section 3.1.3 described the process in determining the maximum force used specifically for the NB4 cells. A force of 0.5 nN was applied to extract the Young's modulus of both untreated and ATO treated NB4 cells. For such a small force, full indentation lengths were used to fit the deflection-displacement curves. The outcome of understanding and perfecting this analysis protocol contributed to obtaining various comparative cell mechanics results. The proper experimental conditions and parameters were then used to determine drug-induced NB4 cell elasticity changes by AFM.

Once the optimized procedures for AFM data collection and the automated data processing code were developed, in Section 3.2, ATO treatment induced alterations of NB4 cell viability, morphology and elasticity were assessed and correlated. As ATO was effective on APL cells through its ability to induce apoptosis, relations between cell viability, morphology and elasticity can be linked through the identified apoptosis stages.

Viability tests using Trypan Blue and LIVE/DEAD viability kit involving ethidium and calcein AM labelling, provided guidelines in identifying a workable ATO concentration of 30 μM, for experiments to be conducted in a reasonable time frame. A drastic increase of the dead cell population was observed between 6 and 24 h post-treatment. Results reported a larger red fluorescence intensity reading at 24 h post-treatment as binding between EthD-1 and DNA increased, suggesting the existence of a large number of nucleus fragmentation (karyorrhexis). A specific period involved drastic changes that could also be identified through both viability assays and elasticity measurements, for example, between 6 and 24 h post-treatments, in

response to the drug effects. With respect to cell morphology, visual inspections on cell size changes were carried out between 0 and 12 h post-treatments, resulting in the observations of cell shrinkage; and cell fragmentation and blebbing could be identified between 24 and 48 h post treatments. However, cell diameter measurements were limited by the cell irregular shape at the later treatment stages. Young's modulus measurements on the other hand revealed an increase in cell elasticity up to 12 h post-treatment. The drop in elasticity observed between 12 and 24 h post-treatment indicated the breakage of the cell membranes and the release of pressure in the cell.

In summary, fluorescence assay measurements have proven that larger dead populations of NB4 cells were found at 24 h post-treatment using 30 μM ATO, indicating the occurrence in cell fragmentation (in the presence of DNA). This is in good agreement with the decrease in Young's modulus measured by AFM and the morphology assessment using optical microscopy. These correlated results between different measurement methods may reveal a potential drug screening approach, for understanding specific physical and biological of drug effects on the cancer cells.

Contributions of this Thesis are outlined in the following:

1) The precise details of the experimental procedures and data analysis approaches related to non-adherent leukemia cells were outlined, in order to customize and optimize AFM data collection and analysis procedures.
2) Alterations in elasticity of individual NB4 cells were quantified, highlighting the importance of biomechanics for sorting and identifying cancer cells, in order to detect and stage cancer.

3) Viability, morphology and elasticity measurements were correlated, revealing the AFM as a potential drug screening approach, for understanding specific physical and biological drug effects on the cancer cells.

4.2 Prospective and Future Work

More adjustments can be implemented in the analysis code in order to increase its speed and accuracy. After reproducing more consistent results on NB4 cells, future work will involve further assessments of NB4 cell elasticity changes when treated with different drugs, such as ATRA and ATRA combined with ATO. Such assessment will show the potential of cell elasticity measurements using AFM as a drug screening and cancer staging tool.

Additionally, in order to link morphology alterations with the microplate fluorescence intensity readings to detect variations in cell viability, fluorescence imaging should be conducted utilizing the same labelling components.

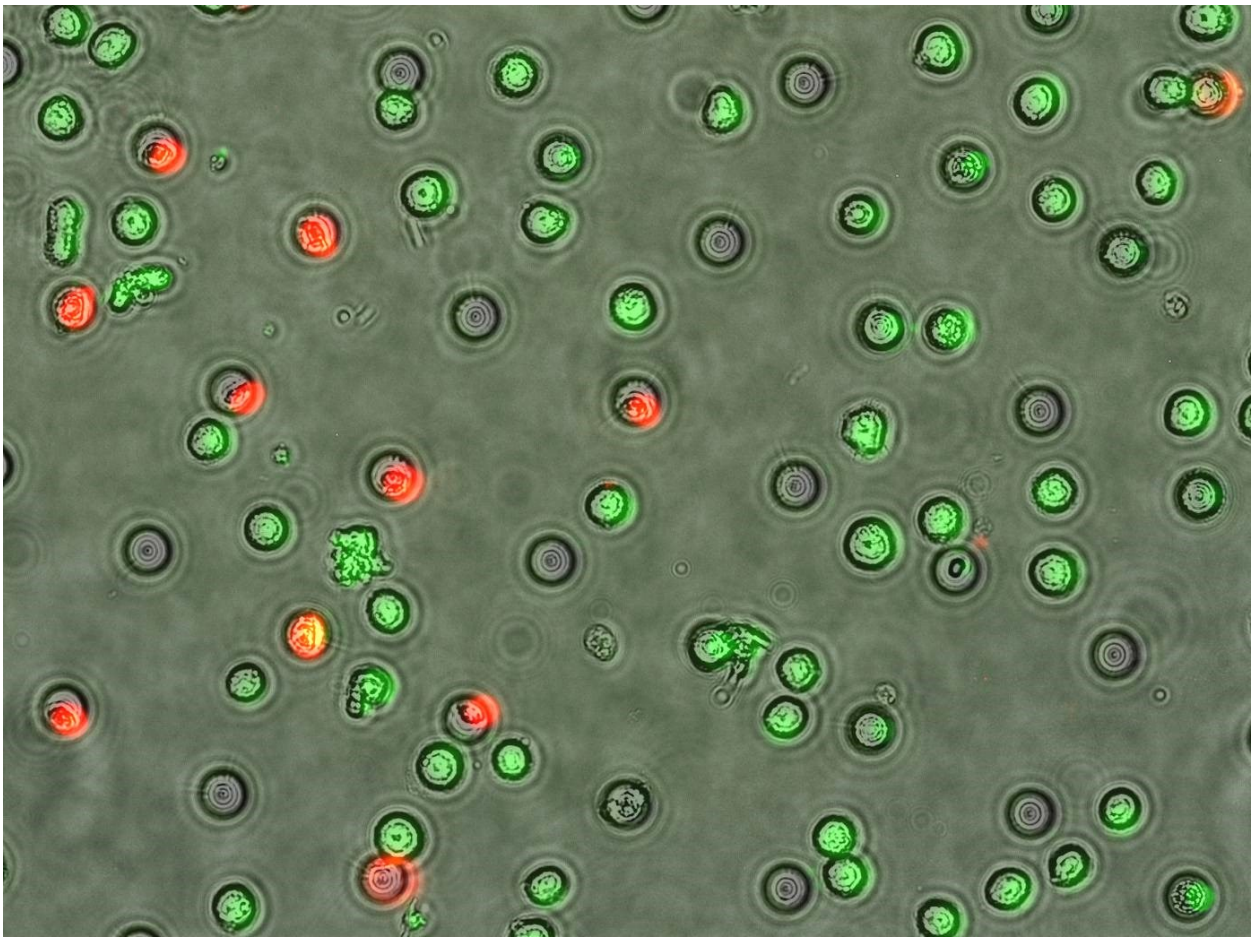

Figure 17. Fluorescence intensity image using LIVE/DEAD imaging kit with EthD-1 and calcein AM as labelling components.

In this context, Figure 17 displays the various cell morphology found within a cell sample. Red fluorescence emission was observed due to the EthD-1 bound to DNA. This may occur during karyorrhexis (fragmentation of the nucleus), which is one of the latest stages during apoptosis. The fluorescence imaging technique has enlightened this research in pursuing fluorescence assay measurements using different or complementary labels, in order to pinpoint recorded apoptosis stages. These will help to fully understand the meaning of the viability assays by linking them to specific cell morphology and elasticity alterations. In light of this conclusion, different fluorescence assays, such as caspase-3 assays which may label earlier stages in apoptosis, may be helpful to pinpoint each apoptosis stages.

REFERENCES

(1) Cross, S. E.; Jin, Y.-S.; Rao, J.; Gimzewski, J. K. Nanomechanical Analysis of Cells from Cancer Patients. *Nat. Nanotechnol.* **2007**, *2* (12), 780–783.

(2) Huang, H.; Kamm, R. D.; Lee, R. T. Cell Mechanics and Mechanotransduction: Pathways, Probes, and Physiology. *Am. J. Physiol. Cell Physiol.* **2004**, *287* (1), C1–C11.

(3) Li, Q. S.; Lee, G. Y. H.; Ong, C. N.; Lim, C. T. AFM Indentation Study of Breast Cancer Cells. *Biochem. Biophys. Res. Commun.* **2008**, *374* (4), 609–613.

(4) Walter, N.; Busch, T.; Seufferlein, T.; Spatz, J. P. Elastic Moduli of Living Epithelial Pancreatic Cancer Cells and Their Skeletonized Keratin Intermediate Filament Network. *Biointerphases* **2011**, *6* (2), 79–85.

(5) Chaudhuri, O.; Koshy, S. T.; Branco da Cunha, C.; Shin, J.-W.; Verbeke, C. S.; Allison, K. H.; Mooney, D. J. Extracellular Matrix Stiffness and Composition Jointly Regulate the Induction of Malignant Phenotypes in Mammary Epithelium. *Nat. Mater.* **2014**, *13* (10), 970–978.

(6) Suresh, S. Biomechanics and Biophysics of Cancer Cells. *Acta Biomater.* **2007**, *3* (4), 413–438.

(7) Frey, M. T.; Engler, A.; Discher, D. E.; Lee, J.; Wang, Y.-L. Microscopic Methods for Measuring the Elasticity of Gel Substrates for Cell Culture: Microspheres, Microindenters, and Atomic Force Microscopy. *Methods Cell Biol.* **2007**, *83*, 47–65.

(8) Mills, J. P.; Qie, L.; Dao, M.; Lim, C. T.; Suresh, S. Nonlinear Elastic and Viscoelastic Deformation of the Human Red Blood Cell with Optical Tweezers. *Mech. Chem. Biosyst.* **2004**, *1* (3), 169–180.

(9) Powe, A. M.; Das, S.; Lowry, M.; El-Zahab, B.; Fakayode, S. O.; Geng, M. L.; Baker, G. A.; Wang, L.; McCarroll, M. E.; Patonay, G.; et al. Molecular Fluorescence, Phosphorescence, and Chemiluminescence Spectrometry. *Anal. Chem.* **2010**, *82* (12), 4865–4894.

(10) Rosenbluth, M. J.; Lam, W. A.; Fletcher, D. A. Force Microscopy of Nonadherent Cells: A Comparison of Leukemia Cell Deformability. *Biophys. J.* **2006**, *90* (8), 2994–3003.

(11) Wang, Z.-Y.; Chen, Z. Acute Promyelocytic Leukemia: From Highly Fatal to Highly Curable. *Blood* **2008**, *111* (5), 2505–2515.

(12) Lam, W. A.; Rosenbluth, M. J.; Fletcher, D. A. Chemotherapy Exposure Increases Leukemia Cell Stiffness. *Blood* **2007**, *109* (8), 3505–3508.

(13) Wiernik, P. H. *Adult Leukemias*; People's Medical Publishing House: USA, 2001.

(14) Jamieson, C. H. M.; Weissman, I. L.; Passegué, E. Chronic versus Acute Myelogenous Leukemia: A Question of Self-Renewal. *Cancer Cell* **2004**, *6* (6), 531–533.

(15) University of Minnesota Twin Cities. Hematography Maturation Chart http://www1.umn.edu/hema/pages/matchart.html (accessed Feb 11, 2016).

(16) Rosenbluth, M. J.; Lam, W. A.; Fletcher, D. A. Analyzing Cell Mechanics in Hematologic Diseases with Microfluidic Biophysical Flow Cytometry. *Lab. Chip* **2008**, *8* (7), 1062–1070.

(17) Orfao, A.; Ciudad, J.; Gonzalez, M.; Lopez, A.; del Mar Abad, M.; Paz Bouza, J. I.; Cruz, J. J.; Gomez Alonso, A.; San Miguel, J. F. Flow Cytometry in the Diagnosis of Cancer. *Scand. J. Clin. Lab. Investig. Suppl.* **1995**, *221*, 145–152.

(18) Weir, E. G.; Borowitz, M. J. Flow Cytometry in the Diagnosis of Acute Leukemia. *Semin. Hematol.* **2001**, *38* (2), 124–138.
(19) Piyasena, M. E.; Graves, S. W. The Intersection of Flow Cytometry with Microfluidics and Microfabrication. *Lab. Chip* **2014**, *14* (6), 1044–1059.
(20) Lanasa, M. C.; Allgood, S. D.; Volkheimer, A. D.; Gockerman, J. P.; Whitesides, J. F.; Goodman, B. K.; Moore, J. O.; Weinberg, J. B.; Levesque, M. C. Single-Cell Analysis Reveals Oligoclonality among "low-Count" Monoclonal B-Cell Lymphocytosis. *Leukemia* **2009**, *24* (1), 133–140.
(21) Rosenbluth, M. J. Probing the Role of Single Cell Mechanics in Disease with Atomic Force Microscopy and Microfluidics. Ph.D. Thesis, University of California, Berkeley: CA, United States, 2008.
(22) Meng, R.; Zhou, J.; Sui, M.; Li, Z.; Feng, G.; Yang, B. Arsenic Trioxide Promotes Mitochondrial DNA Mutation and Cell Apoptosis in Primary APL Cells and NB4 Cell Line. *Sci. China Life Sci.* **2010**, *53* (1), 87–93.
(23) Hoffman, B. D.; Crocker, J. C. Cell Mechanics: Dissecting the Physical Responses of Cells to Force. *Annu. Rev. Biomed. Eng.* **2009**, *11*, 259–288.
(24) Moeendarbary, E.; Harris, A. R. Cell Mechanics: Principles, Practices, and Prospects. *Wiley Interdiscip. Rev. Syst. Biol. Med.* **2014**, *6* (5), 371–388.
(25) Nau, H.; Blaner, W. *Retinoids: The Biochemical and Molecular Basis of Vitamin A and Retinoid Action*. Springer Science & Business Media, 2012.
(26) Rubio, V.; Calviño, E.; García-Pérez, A.; Herráez, A.; Diez, J. C. Human Acute Promyelocytic Leukemia NB4 Cells Are Sensitive to Esculetin through Induction of an Apoptotic Mechanism. *Chem. Biol. Interact.* **2014**, *220*, 129–139.
(27) Zhao, X.-Y.; Yang, S.; Chen, Y.-R.; Li, P.-C.; Dou, M.-M.; Zhang, J. Resveratrol and Arsenic Trioxide Act Synergistically to Kill Tumor Cells In Vitro and In Vivo. *PLoS ONE* **2014**, *9* (6), 1–9.
(28) Zhang, X.; Qin, N.; Chen, X.; Guo, S. The Influence of Joint Application of Arsenic Trioxide and Daunorubicin on Primary Acute Promyelocytic Leukaemia Cells and Apoptosis and Blood Coagulation of Cell Strain. *Pak. J. Pharm. Sci.* **2015**, *28* (3 Suppl), 1075–1078.
(29) Li, L.; Song, H.; Zhong, L.; Yang, R.; Yang, X.-Q.; Jiang, K.-L.; Liu, B.-Z. Lithium Chloride Promotes Apoptosis in Human Leukemia NB4 Cells by Inhibiting Glycogen Synthase Kinase-3 Beta. *Int. J. Med. Sci.* **2015**, *12* (10), 805–810.
(30) Zhang, G.; Yang, Y.-M.; Meng, W.-T.; Zhou, J. Apoptosis of NB4 cells induced by Tanshinone II A combined with arsenic trioxide. *Sichuan Da Xue Xue Bao Yi Xue Ban* **2010**, *41* (1), 57–61.
(31) Luo, W.-D.; Ren, C.-M.; Zhu, M.; Chen, B.-G.; Li, B.-L.; Dai, M.-Z.; Guo, Q.-Y. Study on NB4 cell apoptosis induced by trichosanthin. *J. Exp. Hematol. Chin. Assoc. Pathophysiol.* **2005**, *13* (2), 278–281.
(32) Holcik, M.; LaCasse, E. C.; MacKenzie, A. E. *Apoptosis in Health and Disease: Clinical and Therapeutic Aspects*. Cambridge University Press, 2012.
(33) Srivastava, R. *Apoptosis, Cell Signaling, and Human Diseases: Molecular Mechanisms*. Springer Science & Business Media, 2007.
(34) Elmore, S. Apoptosis: A Review of Programmed Cell Death. *Toxicol. Pathol.* **2007**, *35* (4), 495–516.

(35) Alberts, B.; Johnson, A.; Lewis, J.; Walter, P.; Raff, M.; Roberts, K. *Molecular Biology of the Cell*, 4th edition. Garland Science: New York, 2002.
(36) Fink, S. L.; Cookson, B. T. Apoptosis, Pyroptosis, and Necrosis: Mechanistic Description of Dead and Dying Eukaryotic Cells. *Infect. Immun.* **2005**, *73* (4), 1907–1916.
(37) Zheng, T.; Yin, D.; Lu, Z.; Wang, J.; Li, Y.; Chen, X.; Liang, Y.; Song, X.; Qi, S.; Sun, B.; et al. Nutlin-3 Overcomes Arsenic Trioxide Resistance and Tumor Metastasis Mediated by Mutant p53 in Hepatocellular Carcinoma. *Mol. Cancer* **2014**, *13*, 1–12.
(38) Zheng, Y.; Zhou, M.; Ye, A.; Li, Q.; Bai, Y.; Zhang, Q. The Conformation Change of Bcl-2 Is Involved in Arsenic Trioxide-Induced Apoptosis and Inhibition of Proliferation in SGC7901 Human Gastric Cancer Cells. *World J. Surg. Oncol.* **2010**, *8*, 1–9.
(39) Walker, A. M.; Stevens, J. J.; Ndebele, K.; Tchounwou, P. B. Arsenic Trioxide Modulates DNA Synthesis and Apoptosis in Lung Carcinoma Cells. *Int. J. Environ. Res. Public. Health* **2010**, *7* (5), 1996–2007.
(40) Parmar, S.; Tallman, M. S. Acute Promyelocytic Leukaemia:a Review. *Expert Opin. Pharmacother.* **2003**, *4* (8), 1379–1392.
(41) Breccia, M.; Cicconi, L.; Minotti, C.; Latagliata, R.; Giannì, L.; Lo-Coco, F. Efficacy of Prolonged Therapy with Combined Arsenic Trioxide and ATRA for Relapse of Acute Promyelocytic Leukemia. *Haematologica* **2011**, *96* (9), 1390–1391.
(42) Tallman, M. S. Arsenic Trioxide: Its Role in Acute Promyelocytic Leukemia and Potential in Other Hematologic Malignancies. *Blood Rev.* **2001**, *15* (3), 133–142.
(43) Lo-Coco, F.; Avvisati, G.; Vignetti, M.; Thiede, C.; Orlando, S. M.; Iacobelli, S.; Ferrara, F.; Fazi, P.; Cicconi, L.; Di Bona, E.; et al. Retinoic Acid and Arsenic Trioxide for Acute Promyelocytic Leukemia. *N. Engl. J. Med.* **2013**, *369* (2), 111–121.
(44) Roboz, G. J. Current Treatment of Acute Myeloid Leukemia. *Curr. Opin. Oncol.* **2012**, *24* (6), 711–719.
(45) Ghavamzadeh, A.; Alimoghaddam, K.; Ghaffari, S. H.; Rostami, S.; Jahani, M.; Hosseini, R.; Mossavi, A.; Baybordi, E.; Khodabadeh, A.; Iravani, M.; et al. Treatment of Acute Promyelocytic Leukemia with Arsenic Trioxide without ATRA And/or Chemotherapy. *Ann. Oncol.* **2006**, *17* (1), 131–134.
(46) Government of Canada, H. C. Scientific Advisory Committee on Oncology Therapies (SAC-OT) - Compilation of Recommendations: Arsenic Trioxide - Health Canada http://www.hc-sc.gc.ca/dhp-mps/prodpharma/activit/sci-com/onco/sacot_ccsot_rec_arsen_triox-eng.php (accessed Nov 9, 2015).
(47) Administration, A. G. D. of H. T. G. ARTG ID 152760 https://www.tga.gov.au/artg/artg-id-152760 (accessed Nov 9, 2015).
(48) Drugs@FDA: FDA Approved Drug Products http://www.accessdata.fda.gov/scripts/cder/drugsatfda/index.cfm?fuseaction=Search.DrugDetails (accessed Nov 9, 2015).
(49) European Medicines Agency - Find medicine - Trisenox http://www.ema.europa.eu/ema/index.jsp?curl=pages/medicines/human/medicines/000388/human_med_001107.jsp&mid=WC0b01ac058001d124 (accessed Nov 9, 2015).
(50) Wang, H.; Chen, X.; Wang, B.; Rong, Z.; Qi, H.; Chen, H. The Efficacy and Safety of Arsenic Trioxide with or without All-Trans Retinoic Acid for the Treatment of Acute Promyelocytic Leukemia: A Meta-Analysis. *Leuk. Res.* **2011**, *35* (9), 1170–1177.

(51) Li, M.; Yang, H.; Wang, C.; Yao, Z.; Gao, Y. Tumor necrosis factor alpha enhances apoptosis of all-trans retinoic acid-induced promyelocytic leukemia cells. *Chin. J. Cell. Mol. Immunol.* **2015**, *31* (7), 869–872, 878.

(52) Xu, X.-H.; Ouyang, J.; Xie, P.-H.; Chen, J.-H. Changes of Activity and Expression of Protein Phosphatase Type 2A during the Apoptosis of NB4 and MR2 Cells Induced by Arsenic Trioxide. *J. Exp. Hematol. Chin. Assoc. Pathophysiol.* **2008**, *16* (5), 1021–1025.

(53) Yoo, E. S. Recent Advances in the Diagnosis and Management of Childhood Acute Promyelocytic Leukemia. *Korean J. Pediatr.* **2011**, *54* (3), 95–105.

(54) Dayyani, F.; Kantarjian, H.; O'Brien, S.; Pierce, S.; Jones, D.; Faderl, S.; Garcia-Manero, G.; Cortes, J.; Ravandi, F. Outcome of Therapy-Related Acute Promyelocytic Leukemia with or without Arsenic Trioxide as a Component of Frontline Therapy. *Cancer* **2011**, *117* (1), 110–115.

(55) Coombs, C. C.; Tavakkoli, M.; Tallman, M. S. Acute Promyelocytic Leukemia: Where Did We Start, Where Are We Now, and the Future. *Blood Cancer J.* **2015**, *5*, 1–9.

(56) Löwenberg, B.; Griffin, J. D.; Tallman, M. S. Acute Myeloid Leukemia and Acute Promyelocytic Leukemia. *Hematol. Educ. Program Am. Soc. Hematol. Am. Soc. Hematol. Educ. Program* **2003**, 82–101.

(57) Lengfelder, E.; Hofmann, W.-K.; Nowak, D. Impact of Arsenic Trioxide in the Treatment of Acute Promyelocytic Leukemia. *Leukemia* **2012**, *26* (3), 433–442.

(58) Estey, E. H. Newly Diagnosed Acute Promyelocytic Leukemia: Arsenic Moves Front and Center. *J. Clin. Oncol.* **2011**, *29* (20), 2743–2746.

(59) Healthcare Professional Site | TRISENOX (arsenic trioxide) injection http://www.trisenox.com/hcp/default.aspx (accessed Nov 10, 2015).

(60) Li, J. K.; Sullan, R. M. A.; Zou, S. Atomic Force Microscopy Force Mapping in the Study of Supported Lipid Bilayers. *Langmuir* **2011**, *27* (4), 1308–1313.

(61) Kuznetsova, T. G.; Starodubtseva, M. N.; Yegorenkov, N. I.; Chizhik, S. A.; Zhdanov, R. I. Atomic Force Microscopy Probing of Cell Elasticity. *Micron* **2007**, *38* (8), 824–833.

(62) Kirmizis, D.; Logothetidis, S. Atomic Force Microscopy Probing in the Measurement of Cell Mechanics. *Int. J. Nanomedicine* **2010**, *5*, 137–145.

(63) Lulevich, V.; Zink, T.; Chen, H.-Y.; Liu, F.-T.; Liu, G. Cell Mechanics Using Atomic Force Microscopy-Based Single-Cell Compression. *Langmuir* **2006**, *22* (19), 8151–8155.

(64) Dokukin, M. E.; Sokolov, I. Quantitative Mapping of the Elastic Modulus of Soft Materials with HarmoniX and PeakForce QNM AFM Modes. *Langmuir* **2012**, *28* (46), 16060–16071.

(65) Seifert, J.; Rheinlaender, J.; Novak, P.; Korchev, Y. E.; Schäffer, T. E. Comparison of Atomic Force Microscopy and Scanning Ion Conductance Microscopy for Live Cell Imaging. *Langmuir* **2015**, *31* (24), 6807–6813.

(66) Fischer-Cripps, A. C. *Introduction to Contact Mechanics*, 2nd edition. Ling, F. F., Series Ed.; Mechanical Engineering Series; Springer US: Boston, MA, 2007.

(67) Johnson, K. L. *Contact Mechanics*, 9th edition. Cambridge Univ. Press: Cambridge, 2003.

(68) Lin, D. C.; Dimitriadis, E. K.; Horkay, F. Robust Strategies for Automated AFM Force Curve Analysis--I. Non-Adhesive Indentation of Soft, Inhomogeneous Materials. *J. Biomech. Eng.* **2007**, *129* (3), 430–440.

(69) Guz, N.; Dokukin, M.; Kalaparthi, V.; Sokolov, I. If Cell Mechanics Can Be Described by Elastic Modulus: Study of Different Models and Probes Used in Indentation Experiments. *Biophys. J.* **2014**, *107* (3), 564–575.
(70) Lautenschläger, F.; Paschke, S.; Schinkinger, S.; Bruel, A.; Beil, M.; Guck, J. The Regulatory Role of Cell Mechanics for Migration of Differentiating Myeloid Cells. *Proc. Natl. Acad. Sci. U. S. A.* **2009**, *106* (37), 15696–15701.
(71) Gaman, A.; Osiac, E.; Rotaru, I.; Taisescu, C. Surface Morphology of Leukemic Cells from Chronic Myeloid Leukemia under Atomic Force Microscopy. *Curr. Health Sci. J.* **2013**, *39* (1), 45–47.
(72) Hutter, J. L.; Bechhoefer, J. Calibration of Atomic-Force Microscope Tips. *Rev. Sci. Instrum.* **1993**, *64* (7), 1868.
(73) Lübbe, J.; Temmen, M.; Rahe, P.; Kühnle, A.; Reichling, M. Determining Cantilever Stiffness from Thermal Noise. *Beilstein J. Nanotechnol.* **2013**, *4*, 227–233.
(74) Grattoni, C. A.; Al-Sharji, H. H.; Yang, C.; Muggeridge, A. H.; Zimmerman, R. W. Rheology and Permeability of Crosslinked Polyacrylamide Gel. *J. Colloid Interface Sci.* **2001**, *240* (2), 601–607.
(75) Lee, D.; Rahman, M. M.; Zhou, Y.; Ryu, S. Three-Dimensional Confocal Microscopy Indentation Method for Hydrogel Elasticity Measurement. *Langmuir* **2015**, *31* (35), 9684–9693.
(76) Sen, S.; Subramanian, S.; Discher, D. E. Indentation and Adhesive Probing of a Cell Membrane with AFM: Theoretical Model and Experiments. *Biophys. J.* **2005**, *89* (5), 3203–3213.
(77) Glaubitz, M.; Medvedev, N.; Pussak, D.; Hartmann, L.; Schmidt, S.; Helm, C. A.; Delcea, M. A Novel Contact Model for AFM Indentation Experiments on Soft Spherical Cell-like Particles. *Soft Matter* **2014**, *10* (35), 6732.
(78) Mahaffy, R. E.; Park, S.; Gerde, E.; Käs, J.; Shih, C. K. Quantitative Analysis of the Viscoelastic Properties of Thin Regions of Fibroblasts Using Atomic Force Microscopy. *Biophys. J.* **2004**, *86* (3), 1777–1793.
(79) Harris, A. R.; Charras, G. T. Experimental Validation of Atomic Force Microscopy-Based Cell Elasticity Measurements. *Nanotechnology* **2011**, *22* (34), 345102.
(80) Choi, A. P. C.; Zheng, Y. P. Estimation of Young's Modulus and Poisson's Ratio of Soft Tissue from Indentation Using Two Different-Sized Indentors: Finite Element Analysis of the Finite Deformation Effect. *Med. Biol. Eng. Comput.* **2005**, *43* (2), 258–264.
(81) Trickey, W. R.; Baaijens, F. P. T.; Laursen, T. A.; Alexopoulos, L. G.; Guilak, F. Determination of the Poisson's Ratio of the Cell: Recovery Properties of Chondrocytes after Release from Complete Micropipette Aspiration. *J. Biomech.* **2006**, *39* (1), 78–87.
(82) Maniotis, A. J.; Chen, C. S.; Ingber, D. E. Demonstration of Mechanical Connections between Integrins, Cytoskeletal Filaments, and Nucleoplasm That Stabilize Nuclear Structure. *Proc. Natl. Acad. Sci. U. S. A.* **1997**, *94* (3), 849–854.
(83) Last, J. A.; Liliensiek, S. J.; Nealey, P. F.; Murphy, C. J. Determining the Mechanical Properties of Human Corneal Basement Membranes with Atomic Force Microscopy. *J. Struct. Biol.* **2009**, *167* (1), 19–24.

APPENDIX A: AUTOMATED DATA PROCESSING CODE

```
#pragma rtGlobals=1       // Use modern global access method.
constant k=58.874 //Spring Constant (pN/nm)
constant v = 0.3     //Poisson Ratio
constant R = 10000   //Spherical tip's Radius (nm)
Constant alpha = 35  //Conical tip's angle
//*************************************************************
*
function loadcurve()
Variable Cparam,Cfit, FCF
Variable num_files, ind, num_digits, Z0, d0
Variable j, i, Seq, Zmin, dmin, Zm,dm,w,yo,v,summ,Esum,n, ILmax,
ILmin, PCh,a,gr,ymin,xmin,zind
string name, filename, Pathname, Pathloc, form_file
wave fit_Calc_Ramp_ex_nm
variable graphic, curve_data_pts
dowindow/k table0
dowindow/k graph0
dowindow/k graph1
dowindow/k graph2
dowindow/k graph3
KillWaves/A/Z
Make/D/O Calc_Ramp_Ex_nm, Defl_nm_Ex, Force, Indentation

do
Prompt Cfit, "What Fitting Model would you like to
use?\t1=Spherical\t2=Conical"
DoPrompt "Fitting Model", Cfit
          if(Cfit!=1&& Cfit!=2)
               print "Error, invalid number"
          endif
while(Cfit!=1 && Cfit!=2)
Prompt gr, "Would you like to see the graphs?\t1=yes\t2=no"
DoPrompt "Graphics", gr
     If(gr==1)
     graph1(Cfit)
     graph2(Cfit)
     doupdate
     delayupdate
endif
killwaves/a/z
     switch(Cfit)    // numeric switch
          case 1:         // execute if case matches expression
               do
                    Print "Are the fitting parameters
okay?\rk=",k,"pN/nm\rv=",v,"\rR=",R,"nm\r"
                    Prompt Cparam, "Are the fitting parameters in
the command window okay?\t1=yes\t2=no"
                    DoPrompt "Settings", Cparam
                         if(Cparam!=1 && Cparam!=2)
```

```
                              print "Error, invalid number"
                        endif
                  while(Cparam!=1 && Cparam!=2)
                  break                              // exit from switch
            case 2:         // execute if case matches expression
                  do
                        Print "Are the fitting parameters
okay?\rk=",k,"pN/nm\rv=",v,"\ralpha=",alpha,"°\r"
                        Prompt Cparam, "Are the fitting parameters in
the command window okay?\t1=yes\t2=no"
                        DoPrompt "Settings", Cparam
                              if(Cparam!=1 && Cparam!=2)
                                    print "Error, invalid number"
                              endif
                  while(Cparam!=1 && Cparam!=2)
                  break
            endswitch
      if (Cparam==2)
      return 0
      endif

Prompt num_files, "What is the number of the last indexed file?"
      DoPrompt "Number of files", num_files
      num_files+=1
Prompt num_digits, "How many digits are in the index?"
      DoPrompt "Number of digits", num_digits
      if(num_digits>4||num_digits<0)
      print "Invalid number of digits"
      return 0
      endif
            Make/N=(num_files)/D/O YM_Ramp_vs_Defl, fitting_error_nm,
num_data_pts, Indent_length, contactpoint, Residuals_kPa, curve_num,
YM_Force_vs_Indent        //Create wave to hold Young's Modulus
Values
Prompt Pathloc, "Locate your Path (e.g. P:Raw Data - All -
Trial:ACSII:)"
      DoPrompt "Path Location", Pathloc
      NewPath/O Picoforce Pathloc
prompt name, "What is your files prefix name : (e.g. 13 tip#5-)"
      DoPrompt "File prefix", name
      Prompt ILmin, "Minimum indentation length (nm) = "
      Prompt ILmax, "Maximum indentation length (nm) = "
DoPrompt "Indentation Lenght", ILmin, ILmax
Prompt PCh, "What program have you used?\t1=Picoforce (DI)\t2=JPK"
DoPrompt "Used Program", PCh
      do
      Prompt FCF, "Are you using the approaching (1) or retracting
(2) curve?"
      DoPrompt "Curve fitted", FCF
                  if(FCF!=1&&FCF!=2)
            Print "Please chose between 1or 2"
            endif
```

```
          while(FCF!=1&&FCF!=2)
for(j=0;j<num_files;j+=1)    //Since ''i'' Starts at 0 -->  ''i''
strictly higher than num_files
curve_num[j]=j

if(num_digits==4)
     if(j<10)
     filename =name+"000"+num2str(j)+".txt" // Creates fileprefix +
index + extension file name (txt file)
     elseif(j<100)
     filename =name+"00"+num2str(j)+".txt" // Creates fileprefix +
index + extension file name (txt file)
     elseif(j<1000)
     filename =name+"0"+num2str(j)+".txt" // Creates fileprefix +
index + extension file name (txt file)
     else
     filename =name+num2str(j)+".txt" // Creates fileprefix + index
+ extension file name (txt file)
     endif
elseif(num_digits==3)
     if(j<10)
     filename =name+"00"+num2str(j)+".txt" // Creates fileprefix +
index + extension file name (txt file)
     elseif(j<100)
     filename =name+"0"+num2str(j)+".txt" // Creates fileprefix +
index + extension file name (txt file)
     else
     filename =name+num2str(j)+".txt" // Creates fileprefix + index
+ extension file name (txt file)
     endif
elseif(num_digits==2)
     if(j<10)
     filename =name+"0"+num2str(j)+".txt" // Creates fileprefix +
index + extension file name (txt file)
     else
     filename =name+num2str(j)+".txt" // Creates fileprefix + index
+ extension file name (txt file)
     endif
elseif(num_digits==2)
     filename =name+num2str(j)+".txt" // Creates fileprefix + index
+ extension file name (txt file)
     else
     filename=name+num2str(j)+".txt"

endif

     //Create Columlabels
     GetFileFolderInfo/Z/P=PicoForce filename
if( V_Flag == 0 && V_isFile )   // file exists
     Make/D/O Calc_Ramp_Ex_nm, Defl_nm_Ex, Force, Indentation,
Calc_Ramp_Rt_nm,Defl_nm_Rt
          LoadWave/G/D/W/O/A/L={0,0,0,0,2}/P=PicoForce filename
```

```
	duplicate/O wave0, Calc_Ramp_Ex_nm
	duplicate/O wave1, Defl_nm_Ex

	if(FCF==2)

		invertwave(Calc_Ramp_Rt_nm)
		duplicate/O Calc_Ramp_Rt_nm, Calc_Ramp_Ex_nm
		invertwave(Defl_nm_Rt)
		duplicate/O Defl_nm_Rt, Defl_nm_Ex
		killwaves Defl_nm_rt, Calc_ramp_rt_nm
	Calc_ramp_ex_nm=Calc_ramp_ex_nm*100/100   //TO ARRANGE SCALE
CHAGE MULTIPLICATION NUMBER
	defl_nm_ex=defl_nm_ex/20*20     //TO ARRANGE SCALE CHANGE
MULTIPLICATION NUMBER
		endif

//duplicate/O wave0, Calc_Ramp_Ex_nm
//duplicate/O wave1, Defl_nm_Ex
killwaves wave0,wave1
wavestats Defl_nm_Ex
curve_data_pts = v_npnts
if(PCh==2)
Calc_Ramp_Ex_nm=Calc_Ramp_Ex_nm*-10^9
Defl_nm_Ex=Defl_nm_Ex*10^9
endif
print "Go!0"
Zmin=XYRange(Zmin,dmin,Calc_Ramp_Ex_nm, Defl_nm_Ex, Cfit)
for(i=0;Calc_Ramp_Ex_nm[i]<Zmin;i+=1)     // Initialize
variables;continue test   0,0,0*********************
                                          // Condition;update loop
variables
	endfor
	Z0=Calc_Ramp_Ex_nm[i]
	d0=Defl_nm_Ex[i]
Calc_Ramp_Ex_nm=Calc_Ramp_Ex_nm - Z0
Defl_nm_Ex=Defl_nm_Ex-d0
deletepoints 0, (i), Calc_Ramp_Ex_nm, Defl_nm_Ex

contactpoint[j]=Zmin
wavestats defl_nm_Ex

for(w=v_npnts;abs(Calc_Ramp_Ex_nm[w]-Defl_nm_Ex[w])>ILmax;w-=1)
endfor
deletepoints w,(V_npnts),Calc_Ramp_Ex_nm,Defl_nm_Ex
if(contactpoint[j]!=0)
wavestats defl_nm_Ex
Make/D/N=1/O W_coef, W_sigma, YME, SD, W_sigma2,W_coef2
W_coef[0] = {0.0001}
W_coef2[0] = {0.0001}

switch(Cfit)    // numeric switch
	case 1:         // execute if case matches expression
```

```
	a=3/2
	for(ind=0;ind<v_npnts;ind+=1)
		if(Defl_nm_Ex[ind]<0)
			Defl_nm_Ex[ind] = abs(Defl_nm_Ex[ind])
			endif
		endfor

		FuncFit/NTHR=1/TBOX=768 Sphericalfit W_coef
Calc_Ramp_Ex_nm /X=Defl_nm_Ex /D
		summ=0
		fit_Calc_Ramp_ex_nm = sphericalfit(W_coef,
defl_nm_ex);DelayUpdate
			for(i=0;i<V_npnts;i+=1)
		summ+=(Calc_Ramp_Ex_nm[i]-fit_Calc_Ramp_Ex_nm[i])^2
			endfor
			W_sigma2 = sqrt(summ/v_npnts)
			yo=W_sigma2
			i=v_npnts
		do
		Redimension/N=(V_npnts) force, indentation
			Force = defl_nm_Ex*k
			Indentation = abs(Calc_Ramp_Ex_nm- defl_nm_Ex)
			//wavestats indentation
			//if (indentation[0]>indentation[v_endrow])
			//invertwave(indentation)
			//invertwave(force)
			//zind=indentation[0]
			//indentation[]=indentation-zind
			//endif
			i-=1
			SD=W_sigma2
			YME=W_coef
		deletepoints i, 1,Calc_Ramp_Ex_nm, Defl_nm_Ex,
fit_Calc_Ramp_Ex_nm
			for(ind=0;ind<v_npnts;ind+=1)
		if(Defl_nm_Ex[ind]<0)
			Defl_nm_Ex[ind] = abs(Defl_nm_Ex[ind])
			endif
		endfor
			FuncFit/NTHR=1/TBOX=768 SphereFvsI W_coef2
Force /X=Indentation /D

			FuncFit/NTHR=1/TBOX=768 Sphericalfit W_coef
Calc_Ramp_Ex_nm /X=Defl_nm_Ex /D
				summ=0
			wavestats defl_nm_ex
			redimension/N=(V_npnts)  Calc_Ramp_Ex_nm,
defl_nm_ex,fit_Calc_Ramp_Ex_nm
			fit_Calc_Ramp_ex_nm = Sphericalfit(W_coef,
defl_nm_ex);DelayUpdate
			for(v=0;v<V_npnts;v+=1)
```

```
                              summ+=(Calc_Ramp_Ex_nm[v]-
fit_Calc_Ramp_Ex_nm[v])^2
                        endfor
                        FuncFit/NTHR=1/TBOX=768 Sphericalfit W_coef
Calc_Ramp_Ex_nm /X=Defl_nm_Ex /D
                        W_sigma2 = sqrt(summ/v_npnts)
                        while(abs(Calc_Ramp_Ex_nm[i-1]-Defl_nm_Ex[i-
1])>ILmin&&i>20)      //SD>=W_sigma2&&i>20&&
                        num_data_pts[j]=i
                        Indent_length[j]=Calc_Ramp_Ex_nm[i]-
Defl_nm_Ex[i]
                        YM_Force_vs_Indent[j]=W_coef2[0]*1000
                  Esum=0
                  for(n=0;n<=v_npnts;n+=1)
            Make/O/N=(v_npnts) E1, E2
            if(Defl_nm_Ex[n]==0)
            E1[n]=0
            else
            E1[n]=(((Calc_Ramp_Ex_nm[n]-
Defl_nm_Ex[n])^(3/2)*(sqrt(R)*3)/(4*k*(1-v^2)*Defl_nm_Ex[n]))^(-1))
            endif
            E2[n]=(E1[n]-W_sigma2)^2
      endfor
      Esum=sum(E2,0,v_npnts)

                  break                              // exit from switch
            case 2:         // execute if case matches expression
            a=2
            for(ind=0;ind<v_npnts;ind+=1)
                  if(Defl_nm_Ex[ind]<0)
                        Defl_nm_Ex[ind] = abs(Defl_nm_Ex[ind])
                        endif
                  endfor
            FuncFit/NTHR=1/TBOX=768 Conicalfit W_coef
Calc_Ramp_Ex_nm /X=Defl_nm_Ex /D
                  summ=0
                  fit_Calc_Ramp_ex_nm = Conicalfit(W_coef, defl_nm_ex)
                        for(i=0;i<V_npnts;i+=1)
                  summ+=(Calc_Ramp_Ex_nm[i]-fit_Calc_Ramp_Ex_nm[i])^2
                        endfor
                  FuncFit/NTHR=1/TBOX=768 Conicalfit W_coef
Calc_Ramp_Ex_nm /X=Defl_nm_Ex /D
                        wavestats defl_nm_ex
                        W_sigma2 = sqrt(summ/v_npnts)
                        yo=W_sigma2
                        i=v_npnts
                  do
                  Redimension/N=(V_npnts) force, indentation
                        Force = defl_nm_Ex*k
                        Indentation = abs(Calc_Ramp_Ex_nm-defl_nm_Ex)
                        i-=1
                        SD=W_sigma2
```

```
                        YME=W_coef
                        deletepoints i, 1, Calc_Ramp_Ex_nm,
Defl_nm_Ex,fit_Calc_Ramp_Ex_nm
                        for(ind=0;ind<v_npnts;ind+=1)
                  if(Defl_nm_Ex[ind]<0)
                        Defl_nm_Ex[ind] = abs(Defl_nm_Ex[ind])
                        endif
                  endfor
                  FuncFit/NTHR=1/TBOX=768 ConicalFvsI W_coef2  Force
/X=Indentation /D
                        //W_coef[0] = {0.0001}
                        FuncFit/NTHR=1/TBOX=768 Conicalfit W_coef
Calc_Ramp_Ex_nm /X=Defl_nm_Ex /D
                        summ=0
                        wavestats defl_nm_ex
                        redimension/N=(V_npnts) fit_Calc_Ramp_Ex_nm,
Calc_Ramp_Ex_nm, defl_nm_ex
                        fit_Calc_Ramp_ex_nm = Conicalfit(W_coef,
defl_nm_ex)
                        for(v=0;v<V_npnts;v+=1)
                              summ+=(Calc_Ramp_Ex_nm[v]-
fit_Calc_Ramp_Ex_nm[v])^2
                        endfor
                              W_sigma2 = sqrt(summ/v_npnts)

                  while((Calc_Ramp_Ex_nm[v_npnts-1]-
Defl_nm_Ex[v_npnts-1])>ILmin&&V_npnts>20)
      //SD>W_sigma2&&v_npnts>20&&abs
                        Indent_length[j]=Calc_Ramp_Ex_nm[i]-
Defl_nm_Ex[i]
                        num_data_pts[j]=i
                        YM_Force_vs_Indent[j]=W_coef2[0]*1000
            Esum = 0
            for(n=0;n<=v_npnts;n+=1)
            Make/O/N=(v_npnts) E1, E2
            if(Defl_nm_Ex[n]==0)
            E1[n]=0
            else
            E1[n]=(((Calc_Ramp_Ex_nm[n]-
Defl_nm_Ex[n])^2*(TAN(alpha/360*2*pi)*2)/(PI*k*(1-
v^2)*Defl_nm_Ex[n]))^-1)
            endif
            E2[n]=(abs(E1[n])-YME[0])^2
      endfor
      Esum=sum(E2,0,v_npnts)
                  break
      endswitch

if(YME!=0.0001)
YM_Ramp_vs_Defl[j]=YME[0]*1000 //kPa
fitting_error_nm[j]=SD[0]
```

```
Residuals_kPa[j]=sqrt(Esum)/(v_npnts)/1000
     //sqrt((Esum)/(v_npnts))*1000
else
YM_Ramp_vs_Defl[j]=W_coef[0]*1000 //kPa
fitting_error_nm[j]=W_sigma2[0]
Residuals_kPa[j]=sqrt(Esum)/(v_npnts)/1000
//sqrt(Esum)/(v_npnts)//*1000
endif
endif //if Z0!=0

else //if file does not exist
contactpoint[j]=0
endif//file exists or not

endfor
Edit curve_num,YM_Ramp_vs_Defl, YM_Force_vs_Indent,
fitting_error_nm, Indent_length, num_data_pts, contactpoint,
Residuals_kPa
//filtering curves
wavestats YM_ramp_vs_Defl
for(j=v_endrow;j>=0;j-=1)
if(YM_Ramp_vs_Defl[j]==0)
deletepoints
(j),1,curve_num,residuals_kPa,contactpoint,Indent_length,num_data_pt
s, fitting_error_nm,YM_Ramp_vs_Defl, YM_Force_vs_Indent
//   if(fitting_error_nm[j]>30 || contactpoint[j]==0 ||
Indent_length[j] < ILmin-50|| 0.10*curve_data_pts > num_data_pts[j])
//   do
//   DeletePoints (j),1,
curve_num,residuals_kPa,contactpoint,Indent_length,num_data_pts,
fitting_error_nm,YM_Ramp_vs_Defl, YM_Force_vs_Indent
//   while(fitting_error_nm[j]>30 || contactpoint[j]==0 ||
Indent_length[j] < ILmin-50|| 0.10*curve_data_pts > num_data_pts[j])
     endif
//
endfor
filtercurves()
end
//*****************************************************************

function XYRange(ymin,xmin,Calc_Ramp_Ex_nm, Defl_nm_Ex, Cfit)
Variable Ymin,xmin
wave Calc_Ramp_Ex_nm, Defl_nm_Ex
Variable Cfit
ymin = Calc_Ramp_Ex_nm[0]
     xmin = Defl_nm_Ex[0]

if(Cfit==1 || Cfit==2)
     ymin=contactpt(ymin,xmin, Calc_Ramp_Ex_nm, Defl_nm_Ex, Cfit)
endif
return ymin
end
```

```
//*****************************************************************
function contactpt(ymin, xmin, Calc_Ramp_Ex_nm, Defl_nm_Ex, Cfit)
variable ymin, xmin
wave Calc_Ramp_Ex_nm, Defl_nm_Ex
Variable Cfit
variable q, j, Z2, d2, Z1, d1, Z0,i,d0,a, Ch3, minrange1, maxrange1,
minrange2, maxrange2, Z01,d01
if(Cfit==1)
minrange1=.1
maxrange1=.6

minrange2=.1
maxrange2=.6

elseif(Cfit==2)
minrange1=.1
maxrange1=0.6
minrange2=.1
maxrange2=0.6
endif
Z0=ymin
d0=xmin
ch3=0
do
      ch3+=1
      ymin=Z0
      xmin=d0
      Defl_nm_Ex=Defl_nm_Ex-xmin
      wavestats Defl_nm_Ex
      for (q=v_maxloc;Defl_nm_Ex[q]>maxrange1*v_max;q-=1)
      //Z2 and d2 are placed at 70% of curve
            Z2=Calc_Ramp_Ex_nm[q]
            d2=Defl_nm_Ex[q]
      endfor

      for(j=v_maxloc;Defl_nm_Ex[j]>minrange1*v_max;j-=1)
      //Z1 and d1 are placed at 40% of curve
            Z1=Calc_Ramp_Ex_nm[j]
            d1=Defl_nm_Ex[j]
      endfor

switch (Cfit)
      case 1:
            a=2/3
            break
      case 2:
            a=1/2
            break
endswitch
```

```
Z0 = ((Z2-d2)-(Z1-d1)*(d2/d1)^(a))/(1-(d2/d1)^(a))
      //Calculating contact point
wavestats Calc_Ramp_Ex_nm
if (Calc_Ramp_Ex_nm [v_npnts]>=Z0)
      for(i=0;Calc_Ramp_Ex_nm[i]<=Z0;i+=1) // Initialize
variables;continue test   0,0,0*********************
                  // Condition;update loop variables
      endfor
else
i=v_npnts
endif
      Z0=Calc_Ramp_Ex_nm[i]
      d0=Defl_nm_Ex[i]

while(Z0!=ymin&&ch3<5)

Z01=Z0
d01=d0
ch3=0
do
      ch3+=1
      ymin=Z01
      xmin=d01
      Defl_nm_Ex=Defl_nm_Ex-xmin
      wavestats Defl_nm_Ex
      for (q=v_maxloc;Defl_nm_Ex[q]>maxrange2*v_max;q-=1)
      //Z2 and d2 are placed at 70% of curve
            Z2=Calc_Ramp_Ex_nm[q]
            d2=Defl_nm_Ex[q]
      endfor

      for(j=v_maxloc;Defl_nm_Ex[j]>minrange2*v_max;j-=1)
      //Z1 and d1 are placed at 40% of curve
            Z1=Calc_Ramp_Ex_nm[j]
            d1=Defl_nm_Ex[j]
      endfor

switch (Cfit)
      case 1:
            a=2/3
            break
      case 2:
            a=1/2
            break
endswitch
Z01 = ((Z2-d2)-(Z1-d1)*(d2/d1)^(a))/(1-(d2/d1)^(a))
      //Calculating contact point
wavestats Calc_Ramp_Ex_nm

      if (Calc_Ramp_Ex_nm [v_npnts]>=Z01)
      for(i=0;Calc_Ramp_Ex_nm[i]<Z01;i+=1) // Initialize
variables;continue test   0,0,0*********************
```

```
                                                    // Condition;update loop
variables
      endfor
      else
i=v_npnts
endif
      Z01=Calc_Ramp_Ex_nm[i]
      d01=Defl_nm_Ex[i]

while(Z01!=ymin&&ch3<5)
//if(abs(Z01-Z0)>100)
//Z0=0
//endif

wavestats defl_nm_ex      //THE NEXT 5 LINES MIGHT CAUSE PROBLEMS
FOR CURVES NOT FROM PFQNM!!! MUST BE VERIFIED
for (j=v_endrow;defl_nm_ex[j]>=defl_nm_ex[j-1];j-=1)
endfor

ymin=Calc_ramp_ex_nm[j]
xmin=defl_nm_ex[j]
if (xmin<d0&&ymin>Z0)     //CHANGE CRITERIA FOR ADHESION
Z0=ymin
endif
print Z0
return Z0
end
//*****************************************************************
function deletepts(Calc_Ramp_Ex_nm, Defl_nm_Ex)
wave Calc_Ramp_Ex_nm, Defl_nm_Ex
variable i,j
wavestats Defl_nm_Ex
for (i=0;Calc_Ramp_Ex_nm[i]<=0;i+=1)
          endfor
          j=i-1
deletepoints 0,(j), Calc_Ramp_Ex_nm, Defl_nm_Ex
end
//*****************************************************************
Function Conicalfit(w,d) : FitFunc
      Wave w
      Variable d

      //CurveFitDialog/ These comments were created by the Curve
Fitting dialog. Altering them will
      //CurveFitDialog/ make the function less convenient to work
with in the Curve Fitting dialog.
      //CurveFitDialog/ Equation:
      //CurveFitDialog/ f(d) = d+((pi*k*d*(1-
v^2))/(2*E*tan(alpha*2*pi/360)^(1/2)
      //CurveFitDialog/ End of Equation
      //CurveFitDialog/ Independent Variables 1
      //CurveFitDialog/ d
```

```
	//CurveFitDialog/ Coefficients 1
	//CurveFitDialog/ w[0] = E

	return d+((pi*k*d*(1-v^2))/(2*w[0]*tan(alpha*2*pi/360)))^(1/2)
End

//*****************************************************************
Function Sphericalfit(w,d) : FitFunc
	Wave w
	Variable d

	//CurveFitDialog/ These comments were created by the Curve
Fitting dialog. Altering them will
	//CurveFitDialog/ make the function less convenient to work
with in the Curve Fitting dialog.
	//CurveFitDialog/ Equation:
	//CurveFitDialog/ f(d) = d+((3*k*d*(1-
v^2))/(4*E*SQRT(R)))^(2/3)
	//CurveFitDialog/
	//CurveFitDialog/
	//CurveFitDialog/ End of Equation
	//CurveFitDialog/ Independent Variables 1
	//CurveFitDialog/ d
	//CurveFitDialog/ Coefficients 1
	//CurveFitDialog/ w[0] = E

	return d+((3*k*d*(1-v^2))/(4*w[0]*SQRT(R)))^(2/3)
End
//*****************************************************************
Function SphereFvsI(w,a) : FitFunc
	Wave w
	Variable a

	//CurveFitDialog/ These comments were created by the Curve
Fitting dialog. Altering them will
	//CurveFitDialog/ make the function less convenient to work
with in the Curve Fitting dialog.
	//CurveFitDialog/ Equation:
	//CurveFitDialog/ f(a) = 4*E*sqrt(R)*a^(3/2)/(3*(1-v^2))
	//CurveFitDialog/ End of Equation
	//CurveFitDialog/ Independent Variables 1
	//CurveFitDialog/ a
	//CurveFitDialog/ Coefficients 1
	//CurveFitDialog/ w[0] = E

	return 4*w[0]*sqrt(R)*a^(3/2)/(3*(1-v^2))
End

Function ConicalFvsI(w,a) : FitFunc
	Wave w
	Variable a
```

```
     //CurveFitDialog/ These comments were created by the Curve
Fitting dialog. Altering them will
     //CurveFitDialog/ make the function less convenient to work
with in the Curve Fitting dialog.
     //CurveFitDialog/ Equation:
     //CurveFitDialog/ f(a) = 2*E*tan(alpha/360*2*pi)*a^2/(pi*(1-
v^2))
     //CurveFitDialog/ End of Equation
     //CurveFitDialog/ Independent Variables 1
     //CurveFitDialog/ a
     //CurveFitDialog/ Coefficients 1
     //CurveFitDialog/ w[0] = E

     return 2*w[0]*tan(alpha/360*2*pi)*a^2/(pi*(1-v^2))
End
//*****************************************************************
function  graph1(Ch1)
variable Ch1
wave fit_Calc_Ramp_Ex_nm, defl_nm_ex
Display Calc_Ramp_Ex_nm vs Defl_nm_Ex
if(ch1==1)
FuncFit/NTHR=1/TBOX=768 Sphericalfit W_coef  Calc_Ramp_Ex_nm
/X=Defl_nm_Ex /D
else
FuncFit/NTHR=1/TBOX=768 Conicalfit W_coef  Calc_Ramp_Ex_nm
/X=Defl_nm_Ex /D
endif
ModifyGraph
mode(Calc_Ramp_Ex_nm)=2,rgb(fit_Calc_Ramp_Ex_nm)=(0,0,39168);DelayUp
date
ModifyGraph noLabel=2
ModifyGraph mode(Defl_nm_Ex)=2
Label bottom "Deflection (nm)";DelayUpdate
Label left "Ramp (nm)"
ModifyGraph noLabel=0
ModifyGraph lsize=1,rgb(Defl_nm_Ex#1)=(0,0,39168)
TextBox/K/N=CF_Calc_Ramp_Ex_nm
ModifyGraph swapXY=1
ModifyGraph lsize(Calc_Ramp_Ex_nm)=3,lsize(fit_Calc_Ramp_Ex_nm)=1.5,
rgb(fit_Calc_Ramp_Ex_nm)=(0,0,52224);DelayUpdate
DoUpdate
end
//*****************************************************************
function graph2(Ch1)
variable Ch1
Display Force vs Indentation
if(Ch1==1)
FuncFit/NTHR=1/TBOX=768 SphereFvsI W_coef  Force /X=Indentation /D
else
FuncFit/NTHR=1/TBOX=768 ConicalFvsI W_coef  Force /X=Indentation /D
endif
ModifyGraph noLabel=2
```

```
Label left "Force (pN)";DelayUpdate
Label bottom "Indentation (nm)"
ModifyGraph noLabel=0
ModifyGraph  mode(Force)=2,lsize(Force)=3,rgb(fit_Force)=(0,0,52224)
Modifygraph lsize(fit_force)=1.5
TextBox/K/N=CF_Force
MoveWindow 500,22,900,250
DoUpdate
end

//*****************************************************************
function hist()
variable Reorder
Make/N=100/O YM_Ramp_vs_Defl_Hist;DelayUpdate
Make/N=100/O YM_Force_vs_Indent_Hist;DelayUpdate
Wavestats YM_Ramp_vs_Defl
Histogram/B=1 YM_Ramp_vs_Defl,YM_Ramp_vs_Defl_Hist
Histogram/B=1 YM_Force_vs_Indent,YM_Force_vs_Indent_Hist
Display YM_Ramp_vs_Defl_Hist
Appendtograph YM_Force_vs_Indent_Hist
Label left "Probability";DelayUpdate
Label bottom "Young's Modulus (kPa)"
ModifyGraph mode=5,hbFill=6,toMode=1
ModifyGraph rgb(YM_Force_vs_Indent_Hist)=(0,0,39168)
YM_Ramp_vs_Defl_Hist=YM_Ramp_vs_Defl_Hist/v_npnts
YM_Force_vs_Indent_Hist=YM_Force_vs_Indent_Hist/v_npnts
SetDrawEnv textrgb= (0,0,39168);DelayUpdate
DrawText 0.6,0.1,"E Force vs Indentation"
SetDrawEnv textrgb= (65280,0,0);DelayUpdate
DrawText 0.6,0.2,"E Ramp vs Deflection"
Doupdate
do
Prompt Reorder "Would you like to reorder traces?\t1=yes\t2=no"
Doprompt "Traces" Reorder
if(Reorder==1)
ReorderTraces YM_Ramp_vs_Defl_Hist,{YM_Force_vs_Indent_Hist}
endif
Doupdate
while(Reorder==1)
end
//*****************************************************************
function invertwave(w0)
wave w0
variable i
variable data1
wavestats w0
make/n=(v_npnts)/D/O w1
w1=w0
i=0
do
w0[i]=w1[v_endrow-i]
w0[v_endrow-i]=w1[i]
```

```
i+=1
while(i<=V_endrow/2)
end
//*****************************************************************
function filtercurves()
wave YM_Ramp_vs_Defl, Indent_length, YM_force_vs_Indent,num_data_pts
variable sumEramp, sumEforce, sumIndent
variable ErrRamp, ErrForce, ErrInd,a,b,c,i,med,j

wavestats YM_ramp_vs_defl
i=0
j=0
do
if
(YM_ramp_vs_defl[j]/YM_force_vs_Indent[j]>1.1||YM_ramp_vs_defl[j]/YM
_force_vs_Indent[j]<0.95||abs(YM_ramp_vs_defl[j]-
YM_force_vs_Indent[j])>2.5||Indent_length[j]<100||num_data_pts[i]<10
0)
deletepoints
(j),1,curve_num,residuals_kPa,contactpoint,Indent_length,num_data_pt
s, fitting_error_nm,YM_Ramp_vs_Defl, YM_Force_vs_Indent
wavestats YM_ramp_vs_defl
j=0
endif
j=j+1
while(j<v_npnts)

sumEramp=sum(YM_Ramp_vs_Defl)
sumEforce=sum(YM_force_vs_Indent)
sumIndent=sum(Indent_length)
wavestats YM_ramp_vs_defl
ErrRamp = sumEramp/v_npnts
wavestats YM_force_vs_Indent
ErrForce = sumEforce/v_npnts
wavestats Indent_length
ErrInd=sumIndent/v_npnts
wavestats YM_ramp_vs_defl

a=ErrRamp
b=ErrForce
c=ErrInd
med=Median(YM_ramp_vs_defl)

print "\rMax YM =",v_max,"\rMin YM =",v_min,"\rMedian
=",med,"\rAverage YM-Ramp=",a,"\rAverage YM-Force",b,"\rAverage
Indentation Length=",c

end
//*****************************************************************

function filtercurves2()
wave YM_Ramp_vs_Defl, Indent_length, YM_force_vs_Indent
```

```
variable sumEramp, sumEforce, sumIndent,i
variable ErrRamp, ErrForce, ErrInd,  Minindent, Maxindent,
MinFiterr, MaxFiterr
wave fitting_error_nm, Indent_length, curve_num,
residuals_kPa,contactpoint, num_data_pts

sumEramp=sum(YM_Ramp_vs_Defl)
sumEforce=sum(YM_force_vs_Indent)
sumIndent=sum(Indent_length)
wavestats YM_ramp_vs_defl
ErrRamp = sumEramp/v_npnts
wavestats YM_force_vs_Indent
ErrForce = sumEforce/v_npnts
wavestats Indent_length
ErrInd=sumIndent/v_npnts
Print "average fitting error is ", ErrRamp,"nm and average
indentation length is ", ErrInd, "nm"
Prompt MinFiterr, "Minimum fitting error (nm) = "
     Prompt MaxFiterr, "Maximum fitting error (nm) = "
DoPrompt "Fitting error range", MinFiterr, MaxFiterr

Prompt Minindent, "Minimum indentation length (nm) = "
     Prompt Maxindent, "Maximum indentation length (nm) = "
DoPrompt "Indentation length", Minindent, Maxindent
wavestats  fitting_error_nm
for(i=v_npnts;i>=0;i-=1)
if
(fitting_error_nm[i]>=MaxFiterr||fitting_error_nm[i]<=MinFiterr||Ind
ent_length[i]>=Maxindent||Indent_length[i]<=Minindent)
deletepoints
(i),1,curve_num,residuals_kPa,contactpoint,Indent_length,num_data_pt
s, fitting_error_nm,YM_Ramp_vs_Defl, YM_Force_vs_Indent
endif
endfor

end

Function/D Median(w) // Returns median value of wave w
Wave w
Variable result
Duplicate/O w, temp // Make a clone of wave
Sort temp, temp // Sort clone
result = temp[numpnts(temp)/2]
KillWaves temp // Kill clone
return result
End
```